# Application of Infrared Birefringence Imaging for Measuring Residual Stress in Multicrystalline, Quasi-Mono, Dendritic Web, and String Ribbon Silicon for Solar Cells

by

Sergio Castellanos Rodriguez

B.Sc., Mechanical Engineering
University of Arizona (2008)

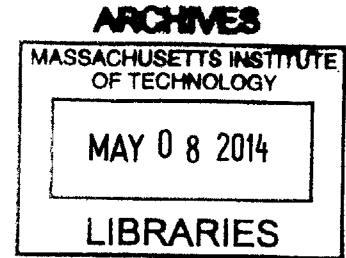
ARCHIVES
MASSACHUSETTS INSTITUTE OF TECHNOLOGY
MAY 0 8 2014
LIBRARIES

Submitted to the Department of Mechanical Engineering
in partial fulfillment of the requirements for the degree of

Master of Science in Mechanical Engineering

at the

MASSACHUSETTS INSTITUTE OF TECHNOLOGY

February 2014

© Massachusetts Institute of Technology 2014. All rights reserved.

Author ........................
Department of Mechanical Engineering
January 17, 2014

Certified by................................
Tonio Buonassisi
Associate Professor of Mechanical Engineering
Thesis Supervisor

Accepted by ..................................
David Hardt, Professor of Mechanical Engineering
Chairman, Department Committee on Graduate Theses

Application of Infrared Birefringence Imaging for Measuring Residual Stress in Multicrystalline, Quasi-Mono, Dendritic Web, and String Ribbon Silicon for Solar Cells

by

Sergio Castellanos-Rodríguez

Submitted to the Department of Mechanical Engineering
on January 17, 2014 in Partial Fulfillment of the
Requirements for the Degree of Master of Science in
Mechanical Engineering

# ABSTRACT

One of the parameters with highest impact on photovoltaic module cost is manufacturing yield during solar cell production. Yield is, to a great extent, directly affected by the crystallization technique used to grow the substrate wafers due to its role in generating residual stresses that can lead to fracture upon wafer processing and handling.

This thesis explores the nature, impact, and a method for quantifying residual stresses in silicon wafers used for solar cells. The combination of an infrared birefringence imaging technique along with a sectioning method is proposed as an approach to spatially resolve and decouple the in-plane residual stress components on four wafers originating from different growth methods. The suitability of this technique is verified, and recommendations for future expansion of this work are presented.

Thesis Supervisor: Tonio Buonassisi

Title: Associate Professor of Mechanical Engineering

# ACKNOWLEDGEMENTS

I can't be thankful enough for all the people that have helped me in one way or another with the completion of this project. I would like to express my gratitude to my advisor Tonio Buonassisi for teaching me how to become a better researcher every day, and by granting me the unique opportunity of doing research in the PV Lab. I am sure if his patience could be translated into kWh, there would be no such thing as energy crisis.

My gratitude goes to Sebastian Oener, Vidya Ganapati, and Stephan Schoenfelder for sharing their knowledge about infrared birefringence imaging. Thanks also go to Douglas Powell, Jim Serdy, Dr. Sanha Kim, Dr. Robert Panas, Dr. Rafael Jaramillo, Dr. Kejie Zhao, Dr. Scott Speakman, Dr. Joshua Guske, and Dr. David Parks for their assistance with equipment design and construction, tool usage, data interpretation, and insightful discussions, which would have made the completion of this work impossible otherwise.

I am also deeply grateful for the discussions, encouragement and assistance from my colleagues David Berney Needleman, Mariela Castillo, Rupak Chakraborty, Riley Brandt, Dylan Erb, Sin Cheng Siah, Dr. Maulid Kivambe, Dr. Mariana Bertoni, Dr. David Fenning, Dr. Joseph Sullivan, Dr. Jasmin Hofstetter, Dr. Hyunjoo Choi, Dr. Mark Winkler, Dr. Vera Steinmann, Dr. Yu-Chieh Lo, Dr. Ernesto Martinez, and the rest of the PV Lab.

I couldn't be luckier with the friends I have made while here at MIT. Their company and support outside the lab have made this a fascinating experience.

Finalmente, gracias a Dios por darme fé y fortaleza en los momentos difíciles. A Pupy por su paciencia y compañía a lo largo de este camino, y a mi familia por las palabras de aliento y el apoyo incondicional en todo momento. Esto es para ustedes.

# CONTENTS


**Abstract** .......... 3

**Acknowledgements** .......... 5

**Contents** .......... 7

**Figures** .......... 11

**Tables** .......... 13

**1 Introduction** .......... 17

- **1.1 Solar Energy Resource** .......... 17
- **1.2 Crystalline Silicon Photovoltaics** .......... 18
- **1.3 Residual Stress** .......... 19
- **1.4 Effects of Residual Stress** .......... 20
- **1.5 Residual Stress in Silicon Growth Methods** .......... 21
  - 1.5.1 Residual Stress in Single-Crystal Silicon .......... 21
  - 1.5.2 Residual Stress in Ingot Casting Silicon .......... 22
  - 1.5.3 Residual Stress in Ribbon Silicon .......... 24
- **1.6 Residual Stress Measurement Techniques** .......... 25
- **1.7 Motivation for Research and Hypothesis** .......... 27

**2 Photoelasticity and Infrared Birefringence Imaging** .......... 29

- **2.1 Birefringence in Solids and Photoelasticity** .......... 29
- **2.2 Grey-Field Polariscope Setup** .......... 31
- **2.3 Stress-Optic Law and Data Interpretation** .......... 34
- **2.4 GFP Software** .......... 37

**3 Measuring Residual Stress via Infrared Birefringence Imaging** .......... 41

- **3.1 Stress Separation** .......... 41
- **3.2 Continuous Sectioning** .......... 42
- **3.3 Sample Selection** .......... 44
- **3.4 Sample Preparation** .......... 45
  - 3.4.1 Surface Smoothening .......... 45

3.4.2 Surface Cutting ........ 47
**3.5 Sample Processing and Analysis. ........ 48**
3.5.1 Experimental Process ........ 48
3.5.2 Analysis Process ........ 49
**3.6 External Validation Techniques ........ 50**
**4 Residual Stress Experimental Results ........ 53**
**4.1 Sample Preparation ........ 53**
4.1.1 Surface Smoothing ........ 53
4.1.2 Surface Cutting ........ 54
**4.2 IBI Residual Stress Results ........ 55**
4.2.1 Dendritic Web ........ 56
4.2.2 String Ribbon ........ 59
4.2.3 Multicrystalline Silicon ........ 62
4.2.4 Quasi-Mono ........ 65
**4.3 XRD Residual Stress Results ........ 68**
**5 Discussion ........ 69**
**5.1 Residual Stress in Silicon Materials ........ 69**
5.1.1 Dendritic Web ........ 69
5.1.2 String Ribbon ........ 70
5.1.3 MC-Si ........ 71
5.1.4 Quasi-mono ........ 72
5.1.5 Comparison ........ 73
5.1.6 XRD Results ........ 73
**6 Future Work ........ 75**
6.1.1 Refinement of Assumptions ........ 75
6.1.2 Applied Load-to-Retardation Calibration ........ 78
6.1.3 FEA Simulation of Alternative Method ........ 79
6.1.4 Software and Polarizer Manipulation ........ 81
**7 Conclusions ........ 83**
**Appendices ........ 84**
**Appendix A. Tool Calibration Steps ........ 85**
**Appendix B. Four Point Bending Device ........ 87**

**Appendix C. Height Impact on Spatial Resolution and Turning On Procedure** .......... **89**
C.1 Height Impact on Spatial Resolution .......... 89
C.2 Tool turning on procedure .......... 90
**Appendix D. DoE Laser Parameters** .......... **91**
**References** .......... **96**

# FIGURES

Figure 1.1 – Residual stress categories outlined over a multicrystalline region. The categories are Macro, Intergranular, and Intragranular residual stress. Figure adapted from Ref. [16] .............. 19
Figure 1.2 - CZ single-crystal growth method. A cross-section top view of the residual pattern is illustrated. Figure adapted from Refs. [20, 22] .............................................................. 22
Figure 1.3 – Calculated temperature distribution (in Kelvin) of two ingot-casting growth methods: Direct Solidification System (DSS) and Heat Exchange Method (HEM). Figure from Ref. [23] .............................................................................................................. 23
Figure 1.4 – Calculated von Mises stress distribution of the ingot after 15 hours of solidification. .................................................................................................................................. 23
Figure 1.5 – a) Schematic of Dendritic Web and b) String Ribbon growth processes. ................ 24
Figure 1.6 – Thermal stress caused by gradients in the cooling profile. Figure from Ref. [32]... 25
Figure 1.7 – Residual stress measuring techniques: 1) Non Destructive, 2) Destructive. ............ 26
Figure 2.1 – Relative retardation through a medium (thickness = d). Figure adapted from Ref. [39] ............................................................................................................................... 30
Figure 2.2 – a) Circular polarized light. b) Elliptical polarized light. Figure adapted from Ref. [39] ............................................................................................................................... 31
Figure 2.3 – Schematic of a Circular polariscope. Adapted from Refs. [42, 43] ......................... 32
Figure 2.4 – GFP architecture with components outlined. Lateral view shows the camera and its holding brackets on a height rail. ......................................................................................... 33
Figure 2.5 – a) Mohr's circle components that can be measured on IBI. b) Redefined stress circle with labels corresponding to the information as given in the IBI software. Note the x-axis is now $2\sigma$. Figures from Ref. [44] and adapted from Ref. [39] .............................................................. 36
Figure 2.6 – Upper ceiling on possible stress values measured at $\lambda$=1100 nm (¼ $\lambda$ Retardation = $\Delta\lambda_{max}$ =275 nm) as a function of sample thickness, and for three different $C$ values. .................. 37
Figure 2.7 – DeltaVision GFP Software with selected windows and buttons highlighted........... 38
Figure 2.8 – DeltaVision GFP Software with the IBI stress components from a Dendritic Web sample analysis ............................................................................................................. 39

Figure 3.1 – (a) Representation of the sample with an elemental unit subjected to principal stresses in the x, and y direction, labeled as $\sigma_1$ and $\sigma_2$, respectively. (b) After freeing a surface, the traction perpendicular to the free surface becomes zero, and any changes in $\sigma_2$ are assumed to be negligible, leading to the assumption and computation of constant $\sigma_2$ values. ........................ 42
Figure 3.2 – Stress tensor components measured by IBI upon creation of free surfaces and differential imaging. Figure from Ref. [44] ........................................................................ 43
Figure 3.3 – Digital photographs of as-grown mc-Si, quasi-mono, String Ribbon, and Dendritic Web wafers with their initial dimensions ........................................................................ 45
Figure 3.4 - CMP tool architecture ........................................................................ 46
Figure 3.5 - Diagram of the experimental work to obtain and isolate different stress tensor components ........................................................................ 49
Figure 3.6 - Process diagram of the analysis procedure to decouple stress components............. 50
Figure 3.7 – Rigaku SmartLab® setup with wafer placed in stage for peak diffraction analysis 51
Figure 4.1 - CMP images of Quasi-Mono and MC-Si, and As-grown String Ribbon and Dendritic Web ........................................................................ 54
Figure 4.2 - Quasi-Mono, MC-Si, String Ribbon, and Dendritic Web wafers after being cut..... 55
Figure 4.3 - a) Infrared transmission image of a Dendritic Web sample with dashed lines representing regions where stress distribution was analyzed via the continuous sectioning method. Lines are numbered 1-6. b) $\sigma_x$-$\sigma_y$ image of the sample prior to cut. c) Image of cut wafer through line 1 subtracted from full wafer to obtain $\sigma_x$. d) Image of cut wafer through line 1 with background subtracted to obtain $\sigma_y$ ........................................................................ 57
Figure 4.4 - Line plots showing the stress distribution profile in Dendritic Web silicon sample: $\sigma_x$-$\sigma_y$ (black), $\sigma_x$ (blue), and $\sigma_y$ (red) at line cuts 1-6 highlighted in Fig. 4.3a .............................. 58
Figure 4.5 a) Infrared transmission image of a String Ribbon sample with dashed lines representing regions where stress distribution was analyzed via the continuous sectioning method. Lines are numbered 1-8. b) $\sigma_x$-$\sigma_y$ image of the sample prior to cut. c) Image of cut wafer through Line 4 subtracted from full wafer to obtain $\sigma_x$. d) Image of cut wafer through Line 4 with background subtracted to obtain $\sigma_y$ ........................................................................ 60
Figure 4.6 - Line plots showing the stress distribution profile in String Ribbon silicon sample: $\sigma_x$-$\sigma_y$ (black), $\sigma_x$ (blue), and $\sigma_y$ (red) at line cuts 1-8 highlighted in Fig. 4.5a.................................. 61

Figure 4.7 a) Infrared transmission image of a mc-Si sample with dashed lines representing regions where stress distribution was analyzed via the continuous sectioning method. Lines are numbered 1-8. b) $\sigma_x$-$\sigma_y$ image of the sample prior to cut. c) Image of cut wafer through Line 4 subtracted from full wafer to obtain $\sigma_x$. d) Image of cut wafer through Line 4 with background subtracted to obtain $\sigma_y$ ........ 63
Figure 4.8 - Line plots showing the stress distribution profile in a mc-Si sample: $\sigma_x$-$\sigma_y$ (black), $\sigma_x$ (blue), and $\sigma_y$ (red) at line cuts 1-8 highlighted in Fig. 4.7a ........ 64
Figure 4.9 a) Infrared transmission image of a quasi-mono sample with dashed lines representing regions where stress distribution was analyzed via the continuous sectioning method. Lines are numbered 1-8. b) $\sigma_x$-$\sigma_y$ image of the sample prior to cut. c) Image of cut wafer through Line 4 subtracted from full wafer to obtain $\sigma_x$. d) Image of cut wafer through Line 4 with background subtracted to obtain $\sigma_y$ ........ 66
Figure 4.10 - Line plots showing the stress distribution profile in a quasi-mono Si sample: $\sigma_x$-$\sigma_y$ (black), $\sigma_x$ (blue), and $\sigma_y$ (red) at line cuts 1-8 highlighted in Fig. 4.9a ........ 67
Figure 5.1 – Comparison of representative line scans from the four different Si samples. Lines correspond to $\sigma_x$-$\sigma_y$ (black), $\sigma_x$ (blue), and $\sigma_y$ (red). Green dashed line represents zero stress. .... 73
Figure 6.1 - breaking the initial stress state into the traction originally present (t), and the traction difference $\Delta t$ (*i.e.*, residual) imposed to lead to the final cut value ........ 75
Figure 6.2 - a) ABAQUS FEA model of Si Dendritic Web wafer with a through-crack in the center. b) Stress distribution upon external loading over the y- and x-axis ........ 79
Figure 6.3 - a) FEA simulation of a crack subjected to loading. b) Closed-form solution from the stress distribution away from a crack. c) Comparison of Analytical and FEA model ........ 80
Figure 6.4 - IBI image of a 3 cm crack introduced in IBI. A progression from an IBI image where no background correction is done, to one with correction is shown. An FEA simulation of the crack is shown to visually match the experimental stress distribution ........ 80
Figure B 1 - Four point bending setup components. a) General setup area (load cell meter not shown), and b) Close up on the bending jig ........ 87
Figure B 2 - a) Beam behavior under four point bending. Line shows the linear stress distribution expected. b) IBI image showing the difference in stress (color-coded) upon loading. c) Line scan from arrow in b) showing the expected stress state transition from a) ........ 88
Figure C 1 - Spatial resolution of imaged area as a function of camera height ........ 89

Figure C 2 - Impact on retardation values of a background image due to the order of operations when turning equipment on ........................................................................................................ 90
Figure D 1 - IBI images of the 9 experiments from the laser optimization DoE.......................... 92
Figure D 2 - Cross-sectional SEM images of the 9 experiments from the laser optimization DoE ........................................................................................................................................ 92
Figure D 3 - Impact (S/N) from each of the parameters on the final stress values from lasering ........................................................................................................................................ 93
Figure D 4 - IBI images of Final lasering optimization for samples 1.1, 1.2, and 1.3 ................ 95

# TABLES

Table A.1 - XRD residual strain and stress calculations for quasi-mono Si sample .................... 68

Table D.1 - DoE with Parameters and Levels varied in this study .............................................. 91

Table D.2 - Experimental parameters and retardation results for three different laser conditions ........................................................................................................................................... 94

CHAPTER

# 1

# INTRODUCTION

The motivation for crystalline silicon (c-Si) solar photovoltaic (PV) devices and limitations of current fabrication methods are outlined in this chapter. This chapter also describes the origin and impact of residual stress from different Si crystallization methods. A review of different techniques to measure residual stress is shown, and lastly, the hypothesis and objective of this work is presented.

## 1.1 Solar Energy Resource

The growing scarcity of fossil fuels such as oil and coal, and their consensus impact on global climate change have raised a global interest in alternative energy sources. From among the variety of options, solar is especially attractive given its potential to meet projected human demand of energy [1]. Among the many direct and indirect advantages of tapping the solar resource, the most important ones concern climate change, the securing of energy supply, and the transformation towards a path of regional energy independence [2].

PV technologies capitalize on the solar potential by directly transforming solar radiation into electricity. Until recently, reports indicate that PV production has been doubling every two years since 2002, increasing at a pace close to 48% each year [3].

Different materials have been explored for PV cells and modules, however c-Si has dominated the market share with close to 90% [4]. Moreover, c-Si PV modules installations have high efficiencies, low technical risk, and low degradation which translates into a grid-competitive levelized cost of electricity (LCOE) with the potential of subsidy-free scale adoption

[5, 6]. All of the aforementioned characteristics place c-Si PV in a position with a promising future ahead to compete against current fossil-based technologies.

## 1.2 Crystalline Silicon Photovoltaics

Silicon is the dominant feedstock material among the different sources used for PV cells and modules. This material dominance derives mainly from an abundance of knowledge transfer from the microelectronics industry into the PV industry; namely knowledge of Si crystals growth and processing of high purity, low-defect density Si wafers.

Low manufacturing costs and PV module prices, paired with high performance and reliability, are fundamental requirements for market expansion and consumer adoption [5, 7]. To meet these requirements, extensive research has been focused toward developing growth methods with high throughput, yield, and efficiency, while at a fraction of the cost of the microelectronics industry's single crystal methods.

Although a number of alternative crystallization methods have accomplished some of the sought features, they come at the expense of creating defects that limit cell performance [8-12]. These growth-related defects not only affect cell efficiency (which is the most important variable affecting module price [13]), but also introduce residual stress into the wafer, directly reducing manufacturing yield [14, 15] (the second most important variable affecting module price [13]).

The main focus of this work is the study of residual stress, which negatively impacts the manufacturing yield when handling and processing of Si wafers [15].

## 1.3 Residual Stress

Residual stress is the stress that remains in a stationary body after processing or manufacturing in the absence of thermal gradients or external forces, and self-equilibrates over a characteristic length that is determined by the stresses origin [16, 17]. In the context of Si crystallization, residual stresses come from the misfit between different regions and the lock-in of defects created due to thermal gradients. These thermal gradients induce strain; if the resulting stress exceeds the yield stress at temperatures above the brittle-to-ductile transition, plastic deformation can result, "locking in" the lattice strain and resulting in residual stress.

Residual stress is conventionally divided into three categories: 1) Macroscopic (macro) stresses, which vary over large distances, 2) Intergranular stresses, which are in the order of the grain size, and 3) Intragranular stresses, which correspond to interface stresses and line defects stress fields, as seen in [16].

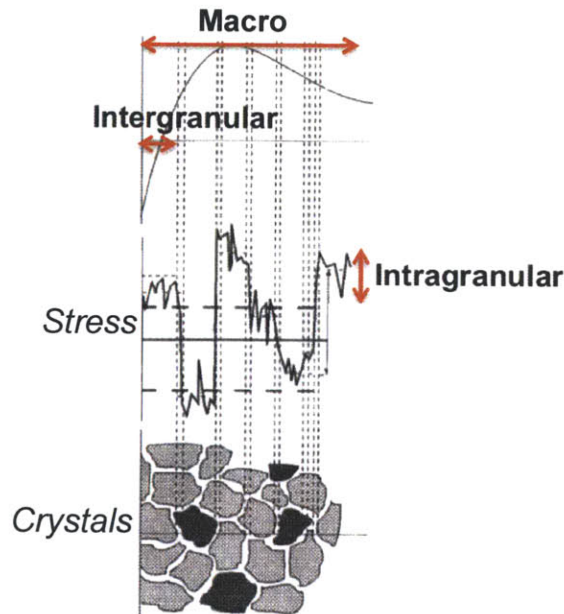


**Figure 1.1 – Residual stress categories outlined over a multicrystalline region. The categories are Macro, Intergranular, and Intragranular residual stress. Figure adapted from Ref. [16]**

During the growth process, macro, intergranular, and intragranular residual stress originates as a consequence of a non-linearity in the time-temperature profile; hence tight growth process control is required to minimize this type of stress. As an example of residual stress minimization, the single-crystal Czochralski (CZ) process can accomplish this goal by reducing the growth (pulling) speed. However, slowing the growth process results in throughput reduction [18].

## 1.4 Effects of Residual Stress

One of the main challenges is to reduce the amount of residual stresses originated upon Si growth and cool down, and cell processing. From the perspective of wafer breakage, residual stress is particularly detrimental when acting on microcracks that arise from the sawing process [19]. Depending on its distribution, residual stress can increase the crack length, leading to fracture propagation and yield losses.

Although some measures are taken to minimize this effect, such as blunting the crack tips by post-sawing chemical etching, there is still a possibility of crack propagation should proper loading conditions (*i.e.*, tensile loading) exist [18]. Hence a need to remove the locked-in loading source, or residual stress, persists.

Moreover, as industry moves towards manufacturing thin wafers, the effect of having low residual stresses becomes more crucial. To explain this, consider Griffith's fracture equation

$$\sigma_{crit} * \sqrt{a} = \sqrt{\frac{2\gamma E}{\pi}} = Constant \tag{1.1}$$

where $\sigma_{crit}$ is the stress required to propagate a crack, $\sqrt{a}$ is the distance from the crack's center to its tip, $\gamma$ is the surface energy, and $E$ is the Young's modulus of the material. From this equation we note that a given crack size will have a maximum possible stress before the fracture propagates. To consider the existing stresses acting on the wafer plane, or in-plane stress conditions, we can state that

$$\sigma_{in\,wafer} = \frac{P_{total}}{A} \tag{1.2}$$

where $P_{total}$ is the in-plane loading condition, and $A$ is the cross-sectional area of the wafer. This loading can be broken down into

$$P_{total} = P_{applied} + P_{residual} \tag{1.3}$$

where $P_{applied}$ can be considered as the applied load during wafer handling, and $P_{residual}$ as the load that comprises residual stress [15].

Fixing the existing load, and comparing two scenarios with varying areas: one in which the existing stress value is exerted on a thin wafer, and one where it acts on a thick wafer, we find that the $\sigma_{in\,wafer}$ will be higher as the area $A$ decreases, as is the case for a thin wafer. In the case of fixed area, and increasing $P_{total}$ by increasing $P_{residual}$ the same result of higher $\sigma_{in\,wafer}$ is obtained. These high $\sigma_{in\,wafer}$ values increase the chance of reaching $\sigma_{crit}$ more rapidly and consequently propagating the existing cracks (assuming mode I fracture).

# 1.5 Residual Stress in Silicon Growth Methods

## 1.5.1 Residual Stress in Single-Crystal Silicon

The CZ single-crystal growth method consists of placing an oriented seed in a molten Si reservoir and slowly pulling it out while counter-rotating the interface between the molten material and growing crystal [20, 21]. The growth conditions of this method leads to a radial stress pattern distribution in some regions of the crystal, as seen in Figure 1.2 [22].

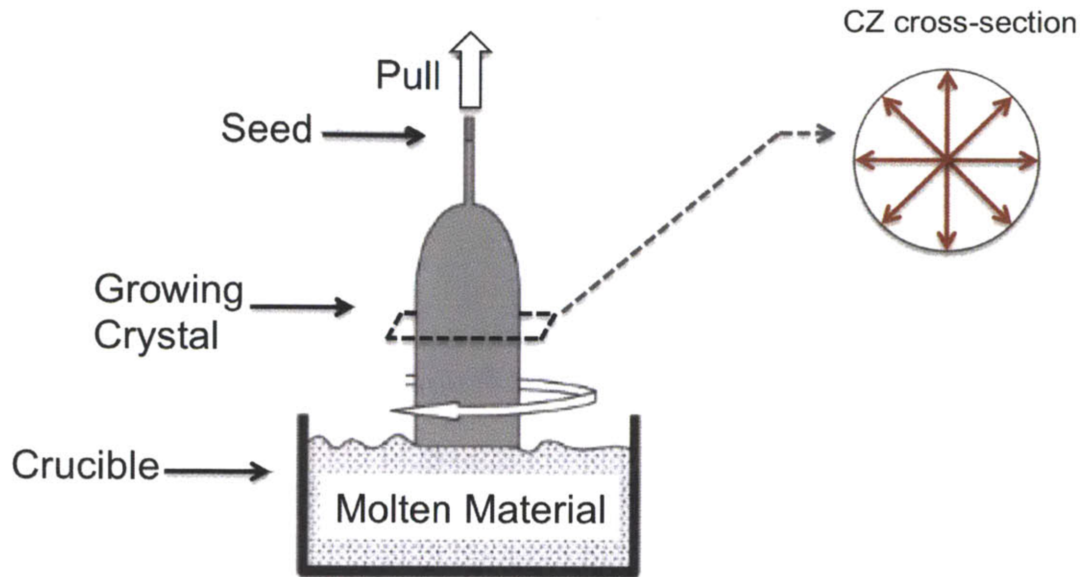


**Figure 1.2 - CZ single-crystal growth method. A cross-section top view of the residual pattern is illustrated. Figure adapted from Refs. [20, 22]**

This method, which is the most mature in the Si industry for growing single crystals, has been refined over the years by tuning growth recipes while designing more efficient hot zones [18]. These changes have reduced line defect density, which in turn, translate into negligible residual stresses in comparison with other growth techniques.

### 1.5.2 Residual Stress in Cast Ingot Silicon

Multicrystalline silicon (mc-Si), which is mainly produced by casting methods, holds a significant portion of the PV cell market share, standing with approximately 50% of the total. Although the efficiency is lower than Si wafers grown from the CZ method, casting process have other advantages such as wider feedstock tolerance, high throughput, and overall lower manufacturing costs [23].

One of the drawbacks of this process is the uneven temperature distribution during ingot cooling, which significantly increases dislocation density [24, 25] and thus introduces residual stresses. A graphical representation of the visibly non-planar temperature distribution in two cast ingot methods can be seen in Figure 1.3.

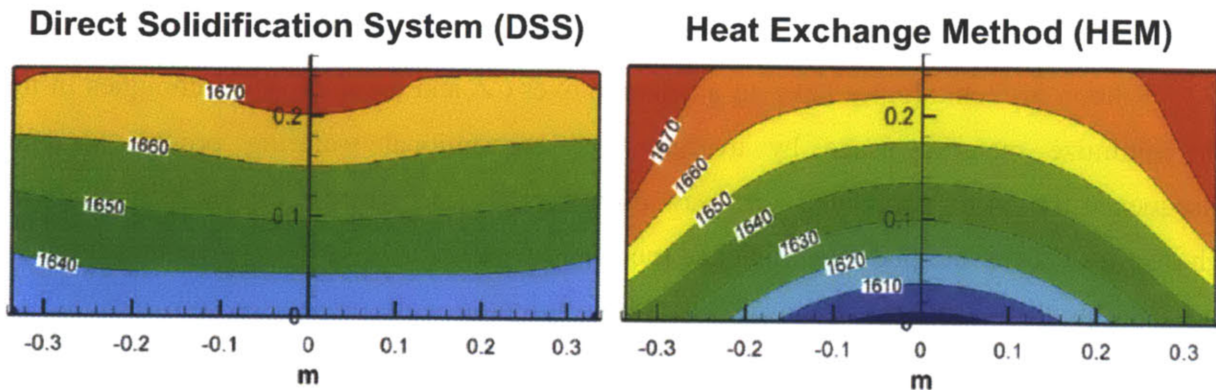


**Figure 1.3 – Calculated temperature distribution (in Kelvin) of two ingot-casting growth methods: Direct Solidification System (DSS) and Heat Exchange Method (HEM). Figure from Ref. [23]**

New variations of the ingot casting methods have emerged in the last years. Such is the case of Quasi-mono, or also known as Mono$^2$, or mono-like Si [26, 27]. This type of ingot-based monocrystalline Si can be produced with a special seed-assisted growth method on a Direct Solidification System (DSS), and with commercial cast furnaces [26-29]. This method, however, is not free from line defects, and thus is hypothesized to contain residual stress, too.

The effect of temperature variation on the stress distribution after the solidification process can be seen in Figure 1.4 for a DSS ingot.

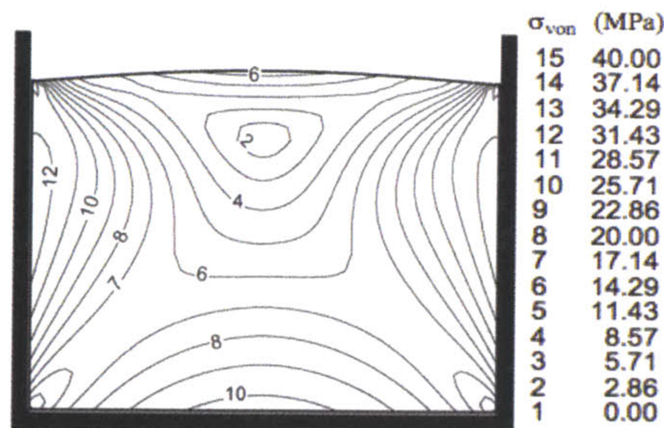


**Figure 1.4 – Calculated von Mises stress distribution of the ingot after 15 hours of solidification. Figure from Ref. [30]**

### 1.5.3 Residual Stress in Ribbon Silicon

Ribbon Si technologies have an advantage over CZ and ingot casting techniques in that they minimize material usage by avoiding the conventional wafering process, and by consequence the >40% associated kerf (saw dust) loss [31]. Challenges of this technology are high overhead costs, and poor electrical and mechanical wafer quality. On the mechanical quality aspect, the gradients in the vertical growth ribbon techniques are responsible for causing high thermoelastic stresses that lead to dislocation nucleation and multiplication, and resulting residual stress [18].

Two vertical ribbon growth processes, Dendritic Web and String Ribbon, are shown in Figure 1.5. Both of these methods are grown directly from the molten Si with no shaping device, except for the strings at the edges. The growth velocity of these methods depends on the latent heat removal rate into the ribbon and of the heat conducted through the melt through the meniscus.

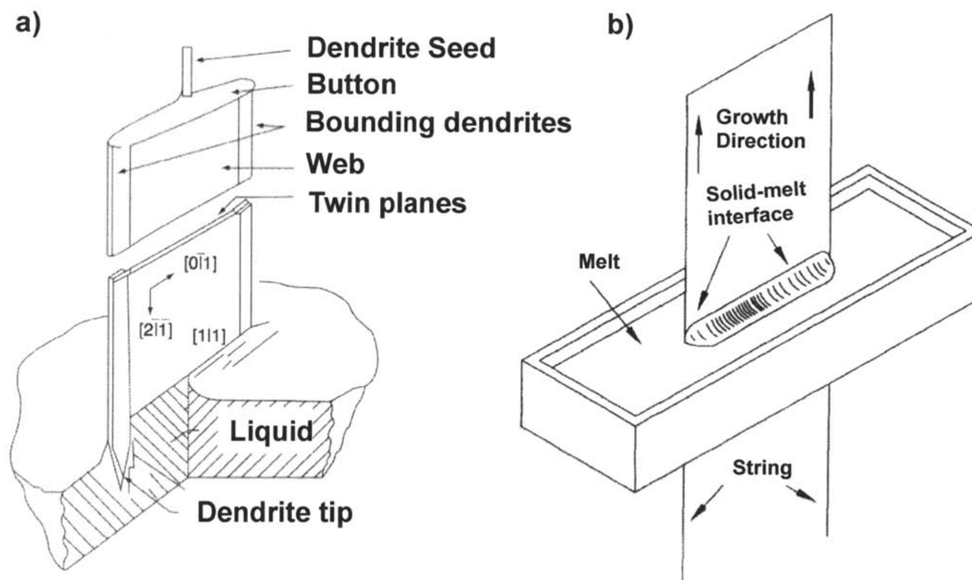


**Figure 1.5 – a) Schematic of Dendritic Web and b) String Ribbon growth processes. Figures from Refs. [18, 32]**

In the case of String Ribbon, the melt temperature has to drop from 1450 °C to ambient within a short distance of the solid-melt interface, introducing a high thermal gradient at the

interface [33]. Moreover, as seen in Figure 1.6, there is a considerable curvature in the cooling profile undergoing for the temperature gradient to decrease to zero at the furnace exit. This gradient translates into thermal stress, which as previously mentioned, if located above the dashed line in the figure (brittle-to-ductile transition temperature), and if exceeding the elastic limit, can induce plastic deformation.

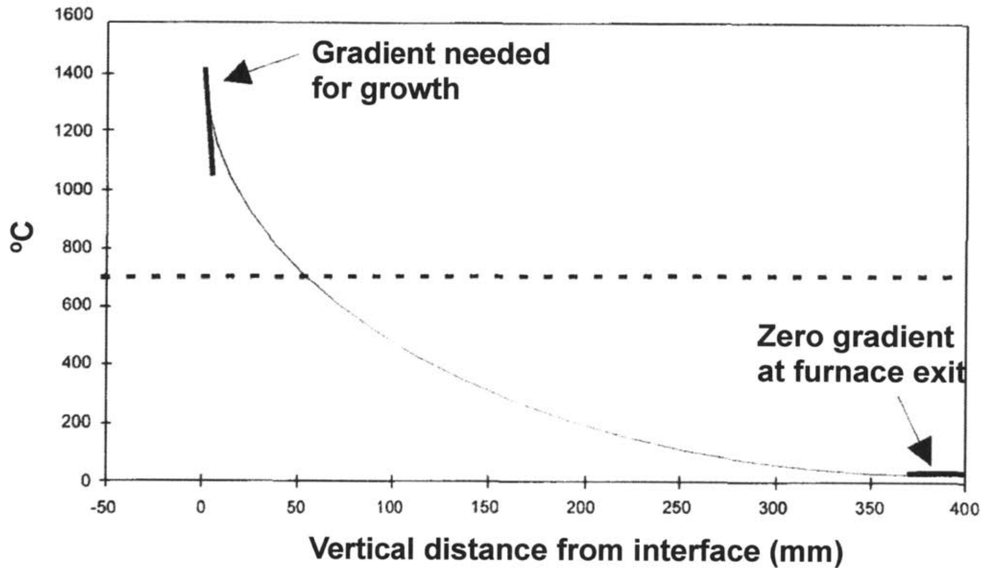


**Figure 1.6 – Thermal stress caused by gradients in the cooling profile. Figure from Ref. [32]**

# 1.6 Residual Stress Measurement Techniques

There is a variety of techniques available to measure residual stress. Broadly speaking, these techniques can be categorized into non-destructive and destructive, as schematically represented in Figure 1.7.

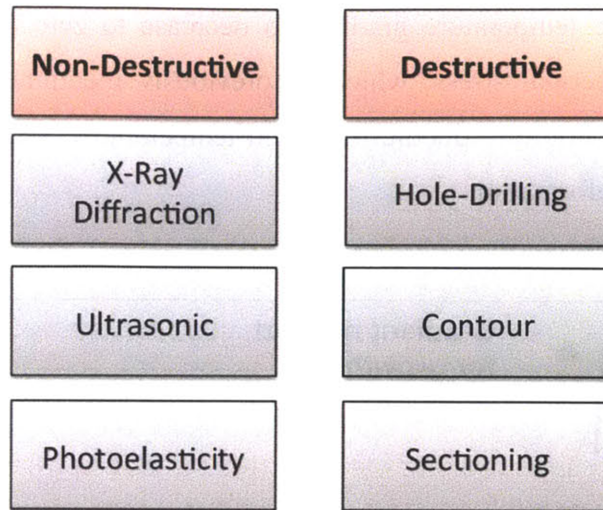


**Figure 1.7 – Residual stress measuring techniques: 1) Non Destructive, 2) Destructive. Figure adapted from Ref. [17].**

A brief description is presented herein, but specific details of each technique can be found elsewhere [17, 34].

In the non-destructive category, three common techniques that can be found are X-Ray diffraction (XRD), photoelasticity, and ultrasonic probing. XRD measures the strain-induced changes in the lattice spacing, which can be projected into different crystal orientations and translated into stresses. In general, the diffracted beam from this technique probes between 10–30 μm deep into the sample and is not a spatially resolved technique. In the resonance ultrasonic vibration (RUV) method, ultrasonic vibrations of a tunable frequency and adjustable amplitude are propagated through the bulk, and are analyzed with an ultrasonic probe [35]. This technique is not spatially resolved and is very sensitive to disturbances in the wave speed originated from crystal orientation or surface imperfections. Photoelasticity is based on measuring the degree of change in light propagation through a material as a consequence of stress. This technique has the potential to be spatially resolved and can detect strains that lead to stresses in the order of <0.1 MPa [33].

In the destructive category, we find (among others) the hole-drilling, contour, and sectioning techniques [36]. The hole-drilling method creates local damage by creating a hole to a depth approximately equal to the hole radius [17]. The surface deformations provide information about the in-plane stresses, which can be obtained with tabulated calibration coefficients. This

technique can prove difficult when interpreting the data, and has only limited strain sensitivity and resolution in the order of the hole drilled. The contour method is one of the more recently develop destructive methods. This method consists on cutting a sample using a wire electric discharge machine (EDM) and then measuring the height profiles of the cut using a laser profilometer. This profile is later input into a finite element simulation to back-calculate the amount of stress required to induce the height profile observed. The contour method relies heavily on high-precision machining, and computational intensive methods [36]. Lastly, the sectioning technique consists of cutting out parts of a specimen while measuring strain relief. In many applications the default strain relief measuring method is *via* strain gauges. This method is most suited for flat specimens and results in the complete destruction of the sample [17, 36].

These different techniques have their own strengths and limitations, which affect their suitability for residual stress analysis in c-Si under different circumstances. Based on the specifications above, the most proper method for use in the laboratory and with potential to transition into a manufacturing line process are thought to be the ones that can obtain spatially resolved stress measurements in a rapid manner.

## 1.7 Research Motivation and Hypothesis

Evidence from the detrimental impact of residual stress in wafers points towards the need to increase yield by monitoring growth and cell processing conditions. Imaging and quantifying the residual stress distribution in crystalline silicon materials can lead to shorter feedback loops in Si wafer growth and processing. Furthermore, spatially resolving the stress distribution can help in better understanding and advancing the knowledge in the current thermo-mechanical models that describe the material's behavior upon different processing conditions.

The hypothesis tested in this work is that the implementation of a non-destructive photoelasticity-based technique, paired with a destructive sectioning technique, is suitable for imaging residual stress distribution across a wafer's width and length. The first technique maps the existing strain in as-grown wafers, and the second technique aids in decoupling the spatially resolved stress into its normal components. This combination of techniques should allow the

measurement of only macro stresses, while eliminating the effects from the intra- and intergranular stresses previously described in Section 1.3.

This combination of methods may serve as a robust method toward inferring cell propensity to mechanical failure in a processing line.

CHAPTER

# 2

# PHOTOELASTICITY AND INFRARED BIREFRINGENCE IMAGING

This chapter discusses the fundamentals of photoelasticity, birefringence, and the infrared birefringence imaging (IBI) technique. The architecture of the grey field polariscope (GFP) to measure birefringence is then described. Lastly, an overview of the software and data interpretation is presented.

## 2.1 Photoelasticity and Birefringence in Solids

Photoelasticity is as an experimental method that determines the stress distribution in a medium by analyzing an induced birefringence phenomenon with polarized light. [37, 38].

Birefringence is an optical property from a material in which the speed of light oriented along one axis travels faster through the medium than the speed of light along another axis. In other words, birefringence is a term used to describe a medium which is doubly refractive in polarized light [38, 39]. When these rays emerge, they are out of phase ($\delta$) and as a consequence of their different propagation velocities the image created carries interference patterns, or fringes, as seen in Figure 2.1 [37]. This condition can be natural, as is the case with calcite crystals, or it can be induced upon lattice straining, as is the case with many materials, among them silicon.

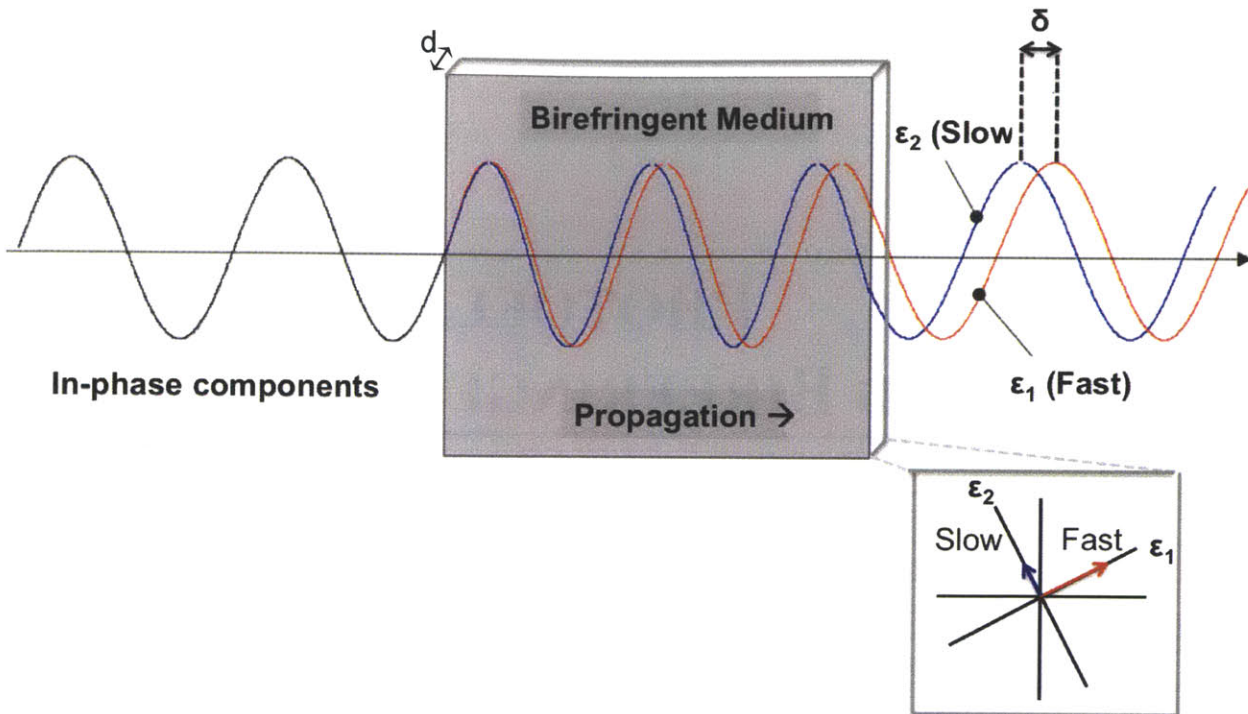


**Figure 2.1 – Relative retardation through a medium (thickness = d). Figure adapted from Ref. [39]**

Principal stresses act in directions normal to their respective principal planes of stress. For an isotropic medium, there is zero shear stress acting in the principal plane, but a maximum shear stress of ½ ($\sigma_1$- $\sigma_2$) in the principal shear plane at 45° to the principal plane of stress [40]. A visual representation of this effect on circular polarized light can be seen in Figure 2.2. The fast axis, labeled *1*, makes angle $\theta$ with a reference direction (*i.e.*, sample). After propagating through the stressed material, the fast axis is in relative retardation with respect to the slow axis, labeled *2,* depicting an ellipse instead of a circle due to the no longer 90° out-of-phase light components. Light amplitude calculations are detailed elsewhere [39][41], however, it should be reemphasized that the major axis of the resulting ellipse is always shifted ¼π away from the location of the principal stress axis.

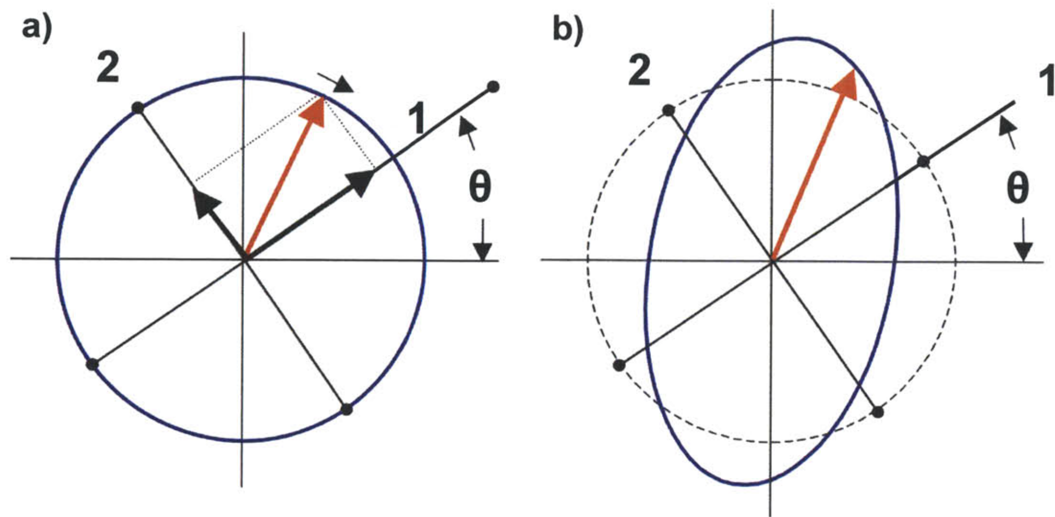


**Figure 2.2 – a) Circular polarized light. b) Elliptical polarized light. Figure adapted from Ref. [39]**

## 2.2 Grey-Field Polariscope and IBI Setup

Birefringence is studied with a polariscope, which is an optical apparatus for polarizing and analyzing light [38]. A schematic of a variation of a circular polariscope, which is the one used in this study, is schematically represented in Figure 2.3. This particular set up is called grey field polariscope (GFP). The reason for it to be called "grey" is due to the cutting of the light beyond the sample boundary, leading to a background that appears of grey color. The grey color falls between dark- and bright-fields, which is a function of the polarizer and analyzer positioning, with respect to the quarter-wave plates [42]. However, this setup has only a rotating analyzer in one of the ends [41].

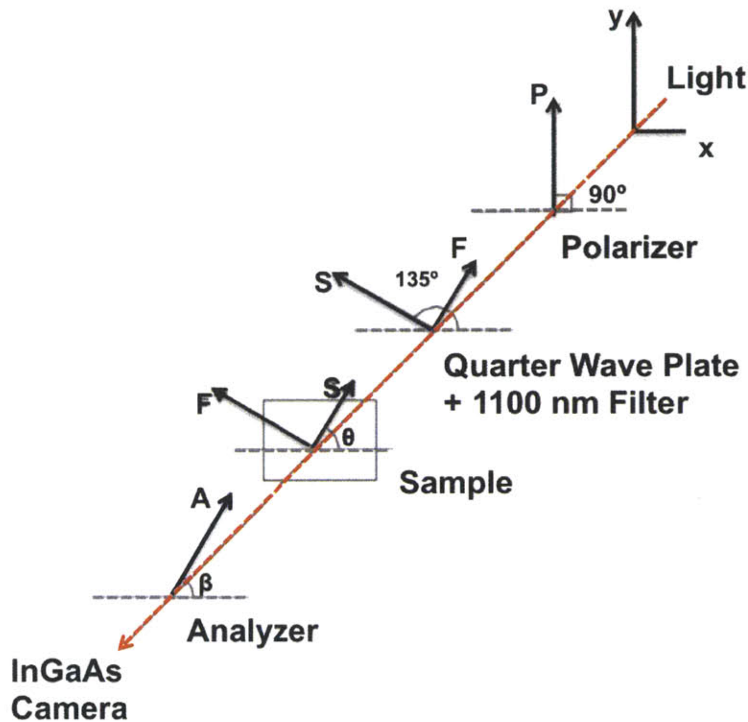


**Figure 2.3 – Schematic of a Circular polariscope. Adapted from Refs. [42, 43]**

This method employs circular polarized light, which consists of two light rays with equal amplitudes vibrating in simple harmonic motion perpendicular to each other, with one component a quarter of a wavelength ahead of the other [38]. Light is initially linearly polarized and then split into two perpendicular vectors by the quarter wave plates, leading to circular polarized light. Since the material analyzed is Si and is transparent to light with wavelengths ≥1100 nm, a narrow band pass filter of 1100 nm is used. The circular polarized light interacts with the strained sample, and as previously described and shown in Figure 2.2, is altered and converted into elliptically polarized light. The analyzer (*i.e.*, a rotating polarizer) is embedded in an InGaAs CCD camera enclosure and examines the locations and magnitude where the light intensity is maximum, and minimum. It rotates while acquiring 16 images per complete revolution, or one image every 22.5°. The images captured at the 16 rotating positions are then used to recreate the ellipse from Figure 2.2, and by consequence, to determine the orientation and magnitude of the principal stresses acting at each pixel of the camera.

By analyzing subtle light intensity changes, this technique can infer the stress state of the material without counting the amount of fringes. That is, the technique can operate in a sub-fringe mode.

The existing GFP setup for IBI is shown in Figure 2.4 and follows the schematic in Figure 2.3 with some additional features.

The setup is arranged vertically. The light source is located at the bottom. Immediately on top are the polarizer, quarter wave plates and band pass filter. The wooden structure seen in the image serves as pillars for the placement of Fresnel lens, should they be needed. Not shown in the image are slits for the placement of a diffuser plate, which is set in place usually unless higher magnification images are required. The translating stage follows afterwards, which contains a glass plate where the sample to analyze is placed. To the right, the light controller is located and set at the same intensity for all measurements. Lastly, the InGaAs camera secured in an enclosure with two locks is shown on top. The camera can adopt different heights by loosening the clamp holders and sliding along the height rails, as seen on the lateral view image.

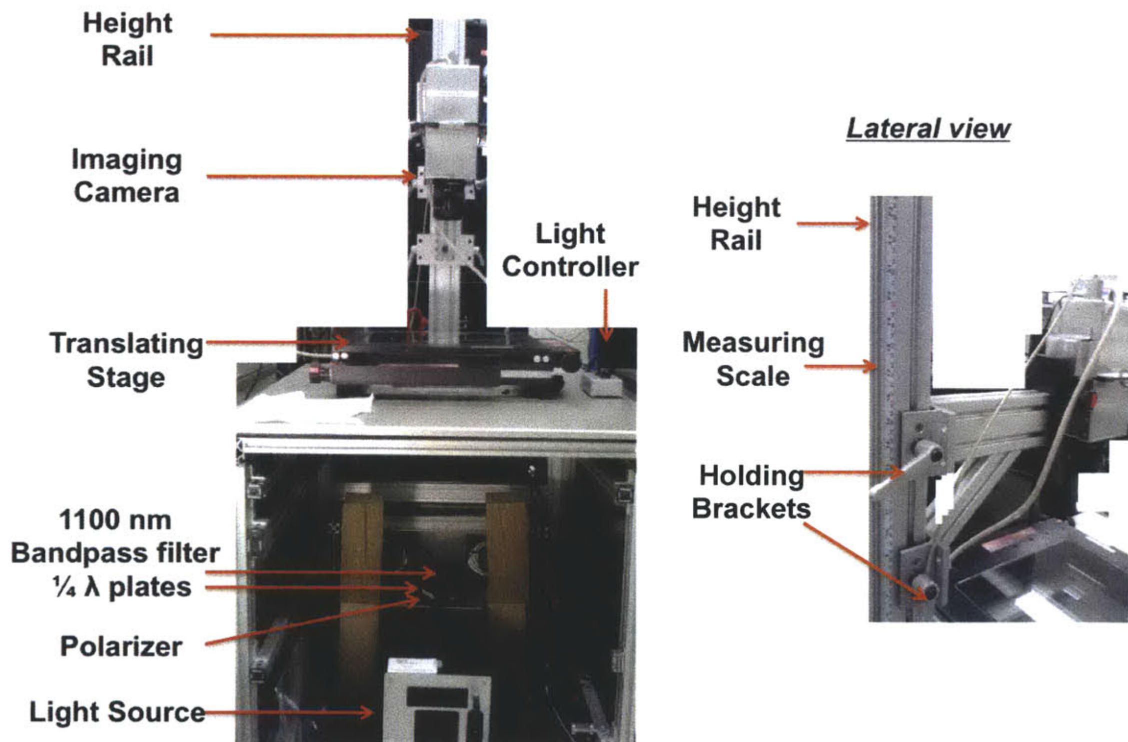


**Figure 2.4 – GFP architecture with components outlined. Lateral view shows the camera and its holding brackets on a height rail.**

After reviewing the principles of birefringence, and the physical instrument to analyze that phenomenon, we now explore the underlying physics that relates light interference to mechanical stress.

## 2.3 Stress-Optic Law and Data Interpretation

As mentioned before, the planes of refraction are related to the directions of the principal planes of stress, and the differences of the propagating ray velocities through the medium are related to the difference between the magnitudes of the principal stresses [37]. In other words, the principal stress directions act as polarizing axes and both light rays travel in the same direction but with different velocities depending on the stress imparted [42].

The index of refraction as it passes through the material is stated in Equation (2.1)

$$n_1 = \frac{c}{v_1} \quad , \quad n_2 = \frac{c}{v_2} \tag{2.1}$$

where $n_1$ and $n_2$ are the indices of refraction for the two directions, $c$ is the speed of light, and $v$ is the propagating speed through the bulk.

For a 2D transparent thin material, the principal components of the refraction indices coincide with the principal components of the stress. This relation is the basis for the stress-optic law, which relates light propagation with induced stress, and states that

$$\begin{aligned} n_1 - n &= (C_1 * \sigma_1) - (C_2 * \sigma_2) \\ n_2 - n &= (C_1 * \sigma_2) - (C_2 * \sigma_1) \end{aligned} \tag{2.2}$$

where $C_1$ is the direct stress-optic coefficient, $C_2$ is the transverse stress-optic coefficient, both with units of $Pa^{-1}$, and $n$ is the refractive index in the unstressed state. From these equations and based on the schematic presented in Figure 2.1, we can obtain the relative phase difference as a function of refractive indices:

$$\delta = \frac{2 * \pi * d}{\lambda}(n_1 - n_2) \tag{2.3}$$

where $\delta$ is the phase difference, and $\lambda$ is the wavelength in units of length. By substituting Equation (2.2) into Equation (2.3), and replacing ($C_1$+$C_2$) by a general material's $C$, we obtain

$$\delta = \frac{2 * \pi * d}{\lambda} * C * (\sigma_1 - \sigma_2) \tag{2.4}$$

Further simplification leads to

$$\Delta\lambda = d * C * (\sigma_1 - \sigma_2) \tag{2.5}$$

which contains the expression $\Delta\lambda$ for retardation in units of length.

It was stated in Section 2.1 that the difference in normal stress components (or shearing), causes a distortion in the circularity of the projected light vectors. As a consequence, the analysis of hydrostatic stress situations (*i.e.*, all normal stress components have equivalent magnitude and direction) is not possible with this method, as this would result in an unaltered perpendicular vectors propagating through the medium and circularly polarized light.

An instructive way of visualizing the measured components from IBI is by referring to Mohr's circle. The use of Mohr's circle is justified under the assumption that a plane-stress condition exists in the sample, which is acceptable for thin wafers. The values acquired from this technique are shown in Figure 2.5a. Shown in Figure 2.5b are the same values with the corresponding nomenclature from the GFP tool's software, which will be detailed in Section 2.4.

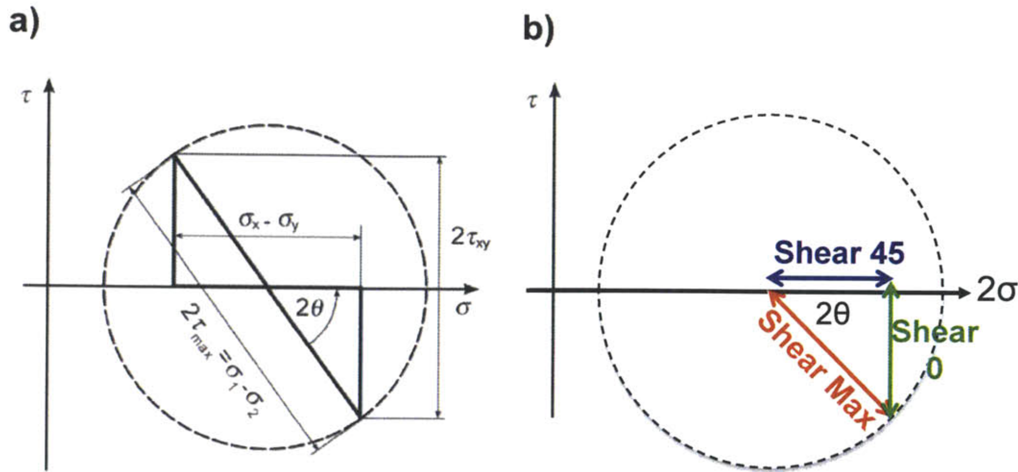


**Figure 2.5 – a) Mohr's circle components that can be measured on IBI. b) Redefined stress circle with labels corresponding to the information as given in the IBI software. Note the x-axis is now $2\sigma$. Figures from Ref. [44] and adapted from Ref. [39]**

The GFP tool performs sub-fringe analysis when the linearity of the relation expressed in Equation (2.5) holds true (*i.e.*, $\Delta\lambda < \frac{1}{4}\lambda$). The possible stress values measured are most importantly a function of the sample thickness, stress optic coefficient, and wavelength. Figure 2.6 shows the upper ceiling of the possible stress measured at $\lambda$=1100 nm. Three different $C$ values, which correspond to three values for the same grain orientation reported in literature, are plotted as a function of thickness to determine the system flexibility. The sensitivity of the measured stress is also a function of wavelength, with the constraint of using light with $\lambda \geq 1100$ nm to avoid absorption in Si.

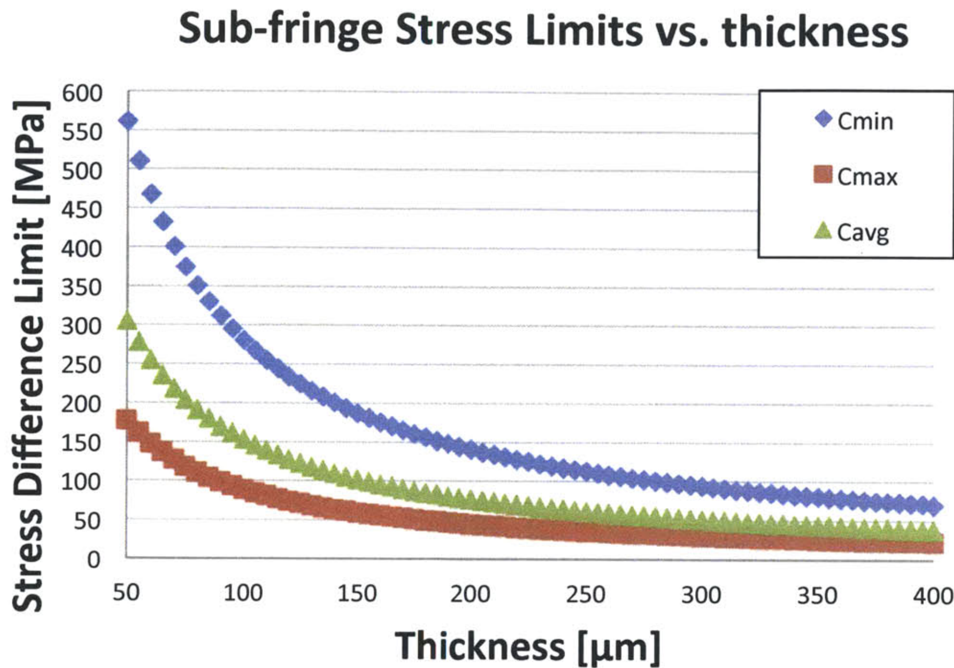


**Figure 2.6 – Upper ceiling on possible stress values measured at $\lambda$=1100 nm (¼ $\lambda$ Retardation = $\Delta\lambda_{max}$ =275 nm) as a function of sample thickness, and for three different *C* values.**

# 2.4 GFP Software

The software used for image acquisition, processing, and analysis is DeltaVision from Stress Photonics®. Extensive details can be found online [45]. To familiarize the reader with the software interface, the main screen with the most commonly used icons and windows are shown in Figure 2.7. The buttons on the upper part correspond to "Imaging", which opens the imaging window and allows to view the camera's input in real time; "Calibration", which opens the calibration window for system calibration (See Appendix A); and "Scale bar Adjustment", which once an image is acquired, allows for manipulation of the limits from the displayed values. Additionally the "Contrast and brightness" window lets the user define the optimum viewing conditions, and the "Acquisition control" window is required for capturing the image being shown in the imaging window. An infrared transmission image of a section from a String Ribbon wafer is shown in Figure 2.7.

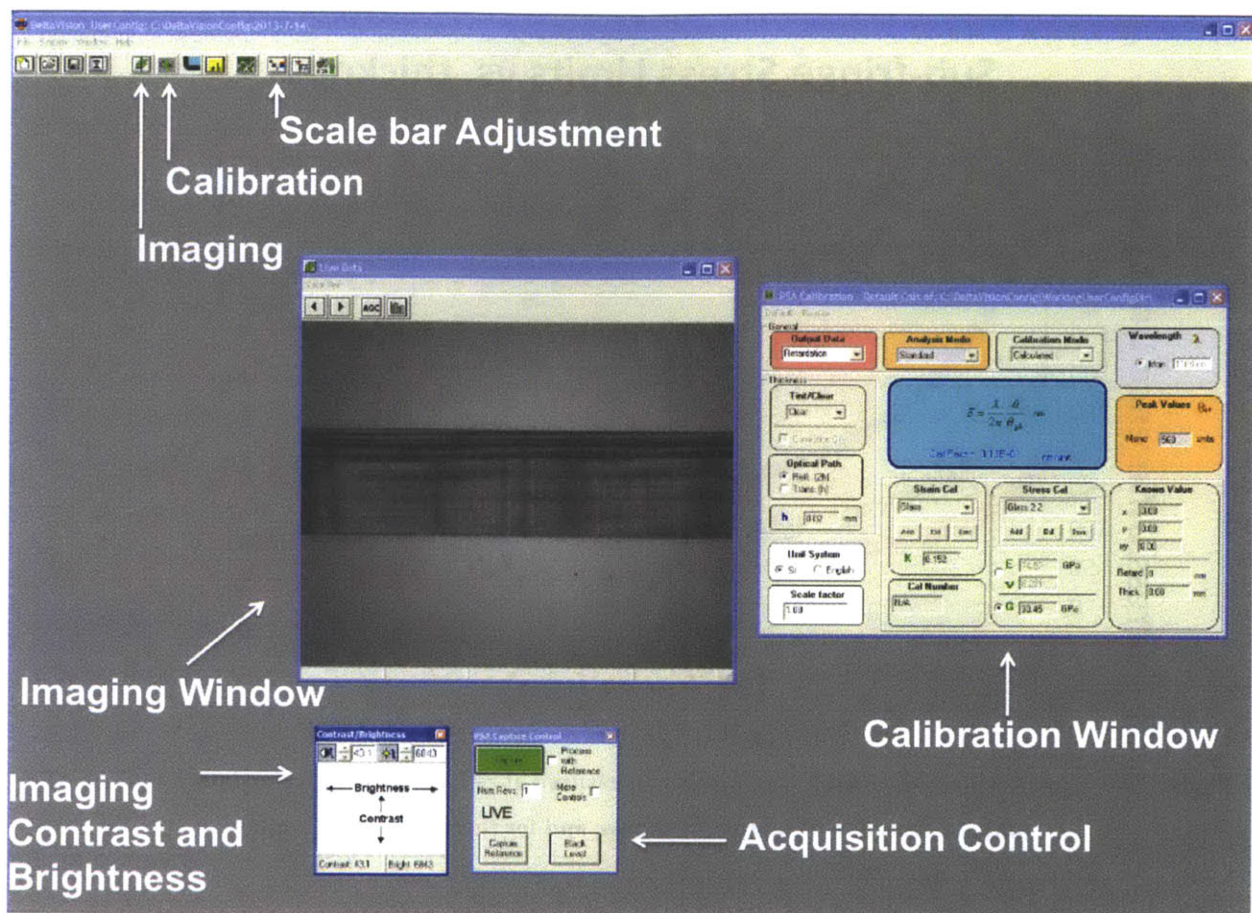


**Figure 2.7 – DeltaVision GFP Software with selected windows and buttons highlighted.**

Once an image is acquired by selecting the number of revolutions in the "Acquisition control" window, the light intensity values are processed and the stress components denoted in the Mohr's circles from Figure 2.5a are shown in Figure 2.8, along with an infrared transmission image.

The evaluated stress components are normal (Shear 45), shear (Shear 0), maximum principal (Shear Max), and orientation (Direction). These components are based in the redefined stress circle from Figure 2.5b. The material seen in the windows from Figure 2.8 is a Dendritic Web sample.

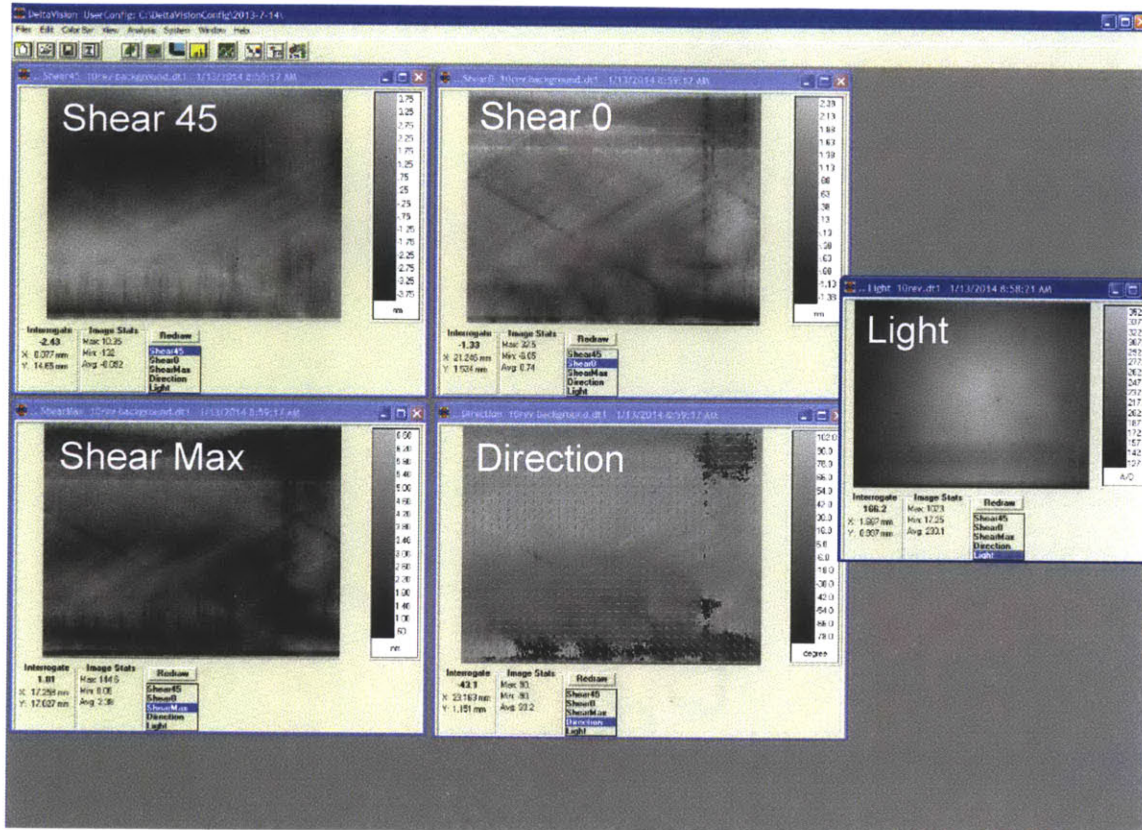


**Figure 2.8 – DeltaVision GFP Software with the IBI stress components from a Dendritic Web sample analysis**

CHAPTER

# 3

# MEASURING RESIDUAL STRESS VIA INFRARED BIREFRINGENCE IMAGING

In the previous chapter, different methods were described for determining residual stress in crystalline materials, including Infrared Birefringence Imaging. Herein, the continuous sectioning method applied to Infrared Birefringence is described, along with the materials selected for this study, their preparation, and the evaluation procedure to decouple normal stress components.

## 3.1 Stress Separation

A limitation of the IBI procedure used in this work is the deconvolution of stress away from the boundaries of the material being analyzed. Existing differential methods start by measuring stress conditions at a boundary, where boundary conditions are known, and then progressing to analyze the stress distribution throughout the sample's width [46]. Other methods consist of rotating the polarizer to track where light extinction occurs, and infer where normal loading is being applied [47, 48]. These methods, however, require either i) a known applied loading, which is not applicable for residual stress analysis, or ii) manipulation of the analyzing polarizer at different angular positions, which is not possible without software modification. A proposed workaround for these limitations is implementing a continuous sectioning method. This method, based on the techniques described in Section 1.6, consists of cutting a sample multiple times to create free surfaces. By creating a free surface, the stress relaxes at the newly formed boundary which contains no perpendicular tractions, and reduce the number of stress components to be solved for. This approach is useful for testing the hypothesis that this method

can be applied to examine residual stress in different Si wafers, decoupling stress into its normal components.

## 3.2 Continuous Sectioning

Continuous sectioning method consists in entirely cutting a portion of the sample off and extracting information from the new boundary from images taken before and after the cut. The free edge consists of only stress components in the direction parallel to the cut direction since the free boundary, or surface perpendicular to the cut's direction, does not have a traction, as seen in Figure 3.1b. The amount of cuts considered depends on the suspected residual stress profile, and the spatial variations one suspects the sample might have.

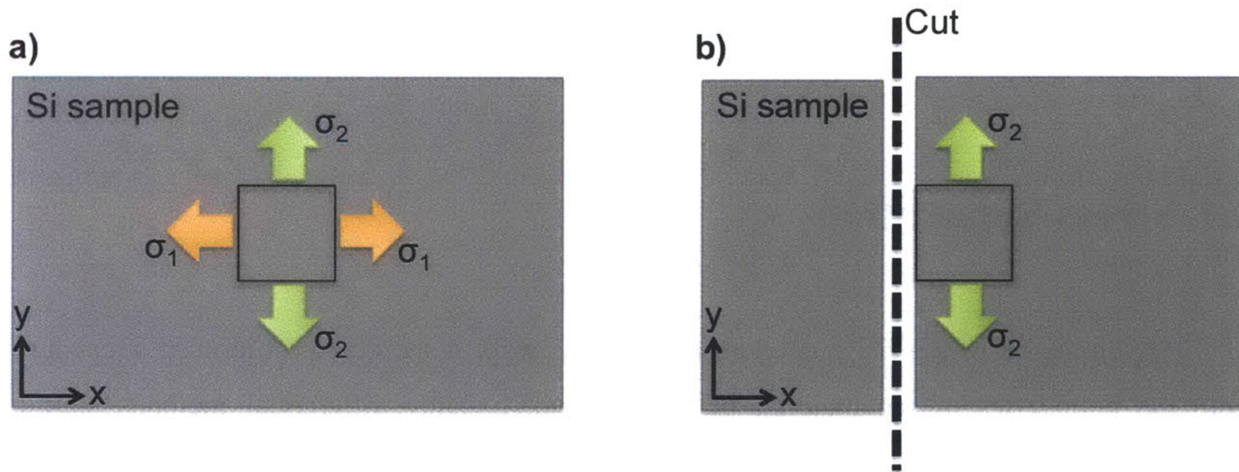


**Figure 3.1 – (a) Representation of the sample with an elemental unit subjected to principal stresses in the x, and y direction, labeled as $\sigma_1$ and $\sigma_2$, respectively. (b) After freeing a surface, the traction perpendicular to the free surface becomes zero, and any changes in $\sigma_2$ are assumed to be negligible, leading to the assumption and computation of constant $\sigma_2$ values.**

Equation (3.1) –the same as Equation (2.5)– shows the retardation value obtained by the GFP tool. This value corresponds to the difference in normal stress components. By cutting and creating a free surface, one can decouple and reduce Eq. (3.1) to Eq. (3.2), which arises from setting $\sigma_1$ to zero and measuring the signal at the edge. Lastly, by taking the difference of

measurements before and after creating a free surface (*i.e.*, subtracting Eq. (3.2) from Eq. (3.1)) we obtain the final Eq. (3.3) which is the component of stress contributing from the x-direction, as seen in Figure 3.1

$$\sigma_1 - \sigma_2 = \frac{\Delta\lambda}{C * d} \tag{3.1}$$

$$0 - \sigma_2 = \frac{\Delta\lambda}{C * d} \tag{3.2}$$

$$(\sigma_1 - \sigma_2) - (-\sigma_2) = \sigma_1 \tag{3.3}$$

Creating a free surface and taking differential images allows the limitation of the GFP tool to measure hydrostatic stress. As before, referring to Mohr's circle, we can see in Figure 3.2 the stress tensor components that the GFP tool can measure with the new approach.

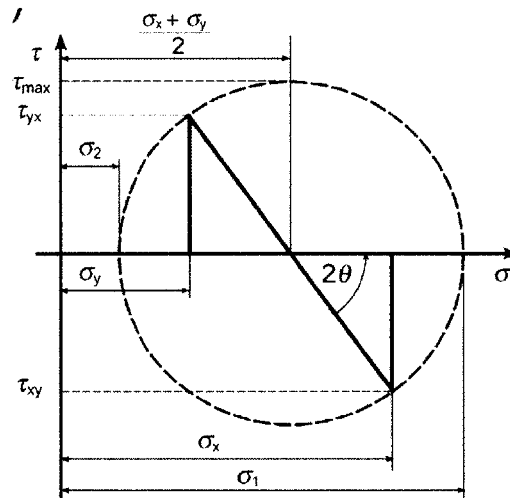


**Figure 3.2 – Stress tensor components measured by IBI upon creation of free surfaces and differential imaging. Figure from Ref. [44]**

In this contribution, we assume that by freeing a surface, the magnitude of the principal stress parallel to the cut (e.g. $\sigma_2$, per Fig. 3.1 convention) remains constant and is not affected by the cut.

This approach differs from other experimental birefringence methods previously reported. In comparison with Ganapati's work [44], this method i) analyzes a broader set of Si samples, and ii) probes a wider spatial distribution per sample to determine stress evolution. Additionally, this approach decouples the effect of purely residual stress from other strain-inducing defects, as well as decouples stress into its normal components, in contrast to the approach reported by Fukuzawa [49].

## 3.3 Sample Selection

A total of four different Si samples from different growth methods were selected for this study. These samples were mc-Si, quasi-mono, Dendritic Web, and String Ribbon. The current dominant industrial Si growth methods are the CZ, and ingot casting, for single and mc-Si, respectively. CZ, however, contains a low amount of residual stress due to its extremely low bulk defect concentration, relative slow growth times, and its lack of crucible walls that can exert stress along the contact interface during cool down [22]. Mc-Si, on the other hand, a more rapid time-temperature profile and crucible walls that lead to the creation of defects and lock-in of residual stress [23]. Therefore, mc-Si proves to be of relevance for this study. A mc-Si sample (210 μm thick) coming from ~50-80% height of the ingot was selected to study its stress distribution. The quasi-mono growth method, which is also an ingot casting method like mc-Si but with single grain orientation seeds, was selected to survey its representative residual stresses. A quasi-mono wafer (205 μm thick) from an ~80% ingot height was chosen. For the third and fourth growth methods, a String Ribbon sample (209 μm thick), and a Dendritic Web sample (110 μm thick) were selected from existing stock in the laboratory. Although String Ribbon and Dendritic Web samples are out of production, they represent interesting case studies due to their relatively high residual stresses, and in the case of Dendritic Web, predictable residual stress pattern [50].

I note that the analysis presented herein is not specific to a particular type of silicon growth method, and can be used for both novel and obsolete methods, as long as it complies with the sample preparation requirements specified next.

## 3.4 Sample Preparation

### 3.4.1 Surface Smoothing

IBI is a transmission technique that requires an adequate amount of light to propagate through the material. Hence, one of the main requirements to conduct experiments with this tool is for a smooth, polished surface.

The as-grown state of mc-Si, quasi-mono, String Ribbon, and Dendritic Web is shown in Figure 3.2. Both mc-Si and mono-like are opaque and do not reflect light, as opposed to the other two samples. The reason for this opaque surface appearance is due to the saw-damage derived from the wafering process [51].

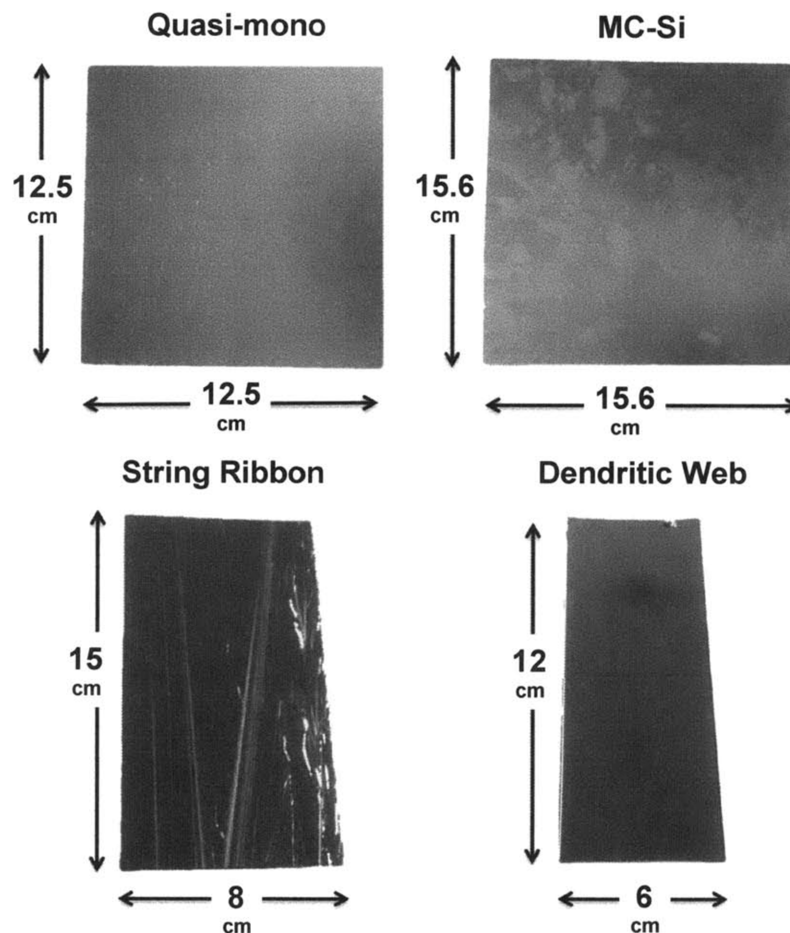


**Figure 3.3 – Digital photographs of as-grown mc-Si, quasi-mono, String Ribbon, and Dendritic Web wafers with their initial dimensions**

A polishing step was performed in mc-Si and quasi-mono wafers to attain the smooth, polished surfaces akin to String Ribbon and Dendritic Web.

To preserve as much in-plane stress as possible for analysis, the constraint for polishing was to maintain sample integrity at all times (*i.e.*, not cutting the wafer into smaller samples). One option was mechanically polishing a full wafer on a Buehler Mechanical Polishing EcoMet® 250 system. For this approach, an aluminum disk of 203.5 mm diameter, 16.2 mm thick, was machined along with proper mounting holes. The Al disk was then placed on a hot plate until reaching 120 °C. Crystalbond™ mounting wax was placed on the surface of the disk, and once melted, the wafer was placed on top.

The second approach considered was chemical-mechanical polishing (CMP). This method consists on flooding the surface with a special chemical solution that paired with a rotating polymer-impregnated fiber pad, smoothens the surface to a mirror-like finish [52].This setup, owned by LMP's Tribology Lab at MIT, can be seen in Figure 3.4.

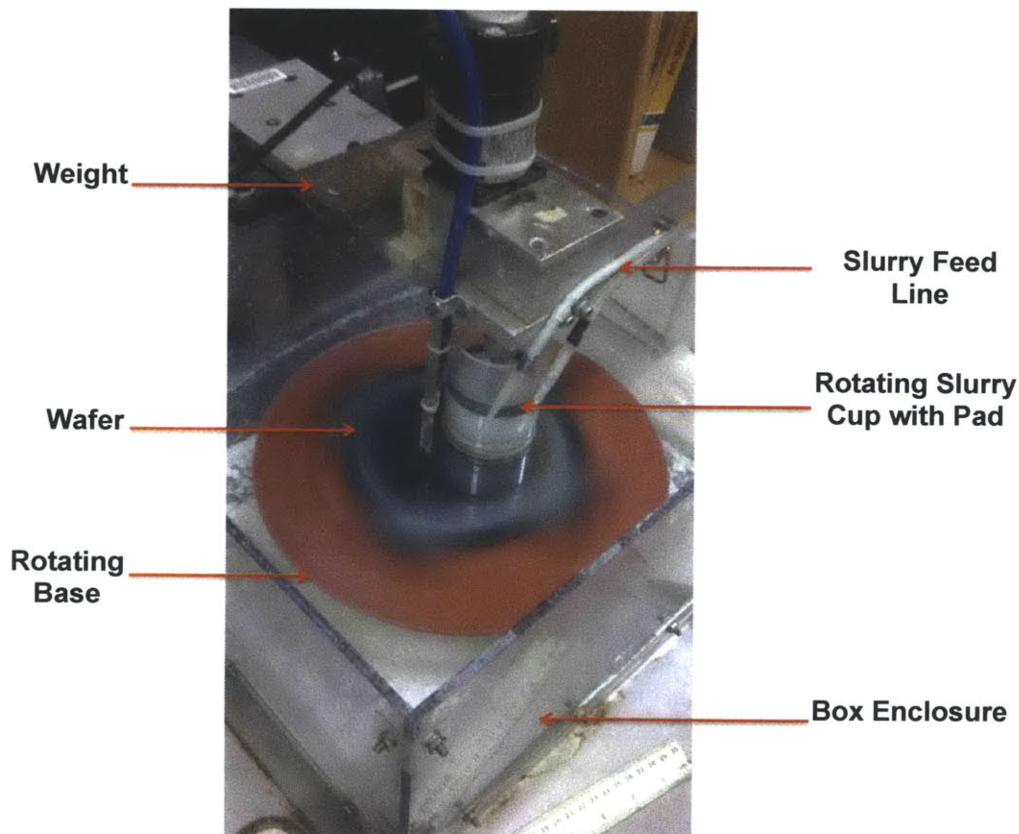


**Figure 3.4 - CMP tool architecture**

A neoprene rubber sheet was placed on the rotating aluminum base, followed by the placement of a 15×15 mm, 10 mm thick square glass that served as support for the wafer. The glass was then covered to its dimension by another thin rubber sheet held by the capillary force of a few droplets sprinkled throughout its surface area. This sheet was then squeezed from above to remove air bubbles. The wafer was then placed on top and pressed against the sheet to ensure proper adhesion. Once the sample was fixed and resisted slight movements, the polishing pad was carefully placed on top, followed by the pumping of the slurry. A Cabot microelectronics chemical slurry was used for this experiment, containing a 3% hydrogen peroxide, and diluted afterwards with water in a 1:1 volumetric ratio. A weight was added on top, resulting in a total of 10.5 KPa stress applied on to the wafer for polishing. Lastly, a gradual increase in matched rotational speed from the base and the pad was done until reaching 110 rpm. At these stated conditions, a total of 3 hours on average was required to polish each mc-Si and quasi-mono wafer side.

### 3.4.2 Surface Cutting

During sectioning, the samples were subjected to a laser-cutting procedure to create free surfaces. The equipment used to cut the silicon samples is an Electrox Raptor Fiber Laser system, with a 1064 nm wavelength. The distance between cuts was 1 cm and the number of cuts for each sample varied depending on the size of the sample and the camera's field of view. In total, the mc-Si sample had 13 vertical cuts, the quasi-mono 11 cuts, the String Ribbon 12 cuts, and the Dendritic Web 8 cuts. Tape markers were placed in the glass substrate inside the laser tool to fix the wafer in a repeatable position. This ensured precision in the separation between cuts. Appendix D shows the design of experiment performed to optimize laser conditions which led to the minimum amount of stress introduced from laser cutting, as measured by the GFP tool. These parameters were: Power = 75%, Laser Pulse width = 120 nm, Frequency = 40 kHz, Rate = 170 mm/s, and cutting Offset = 1.024 μm.

## 3.5 Sample Processing and Analysis.

### 3.5.1 Experimental Process

The height selected for the images taken in this study was 910 mm, which is the distance measured from the lowest part of the camera-holding bracket (marked on the ruler in Figure 2.4) to the glass. This height was selected based on the minimum height that could capture the entire polished area on the biggest wafer (mc-Si wafer).

The process flow to cut and acquire images is shown in Figure 3.5. First, an image of the background was taken at 10 revolutions, which is the amount of full rotations the polarizer in the camera makes. This amount of revolutions provided a good signal-to-noise ratio. The wafer was then placed and centered into its imaging position via three pairs of magnets. These magnets served as a three-point kinematic constraint that ensured the placement of the wafer over the course of the experiment. Once the image was taken (also at 10 revolutions) the sample was transferred to the laser-cutting tool to be cut through its width. With the laser parameters stated before, 15 line repetitions proved enough to cut and separate the cutoff section from the wafer. Then, another image was taken of the remaining portion of the wafer. The reason for taking another image, as previously stated, is that by creating a free surface where there was none before, it is now possible to decouple into normal stress components. Lastly, another background image was taken to account for any deviation in signal that could have arisen from equipment idling.

This procedure was repeated throughout the length of the polished area on all samples, allowing for the extraction of distribution in the residual stress pattern as a function of discrete distances.

**Process Diagram: Experimental**

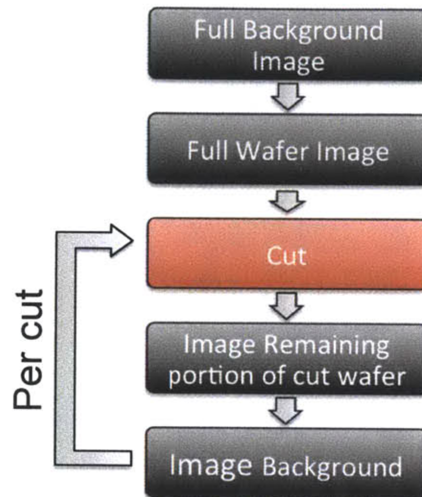


**Figure 3.5 - Diagram of the experimental work to obtain and isolate different stress tensor components**

### 3.5.2 Analysis Process

The process flow to evaluate and decouple $\sigma_x$ and $\sigma_y$ is shown in Figure 3.6. Once sufficient cuts had been made to cover the extent of the imaging area, the files were saved and then exported into MATLAB® for visualization, processing, and plotting. To decouple and obtain the effect of the normal stress component in the x-axis, (*i.e.*, $\sigma_x$) the image of the wafer cut through the y-axis was subtracted from the full wafer image before being cut. This procedure assumed that the changes observed are due to the stress components in the y-axis, now that the normal stress component in the x-axis is null. To then extract the $\sigma_y$ value, the image of the wafer cut through the y-axis was corrected for spurious illumination, as well as glass plate interference effects by subtracting the Background Image. The retardation arising from the difference in normal stress components, or shear, was obtained by correcting the signal of the full wafer prior to cut, *via* subtraction of the background image. Lastly, these values were converted from retardation [nm] to stress [Pa] by the "retardation-to-stress" factor, which is equivalent to 1 / *C***d*, from Eq. 3.1. In this case, the *C* coefficient is optimized for the grain orientation of each surveyed sample, where stress-optic coefficient values were taken as $C_{<100>} = 1.82*10^{-11}$ $Pa^{-1}$, $C_{<111>} = 1.7*10^{-11}$ $Pa^{-1}$. and $C_{<multicrystalline\ average>} = 1.8*10^{-11}$ $Pa^{-1}$.

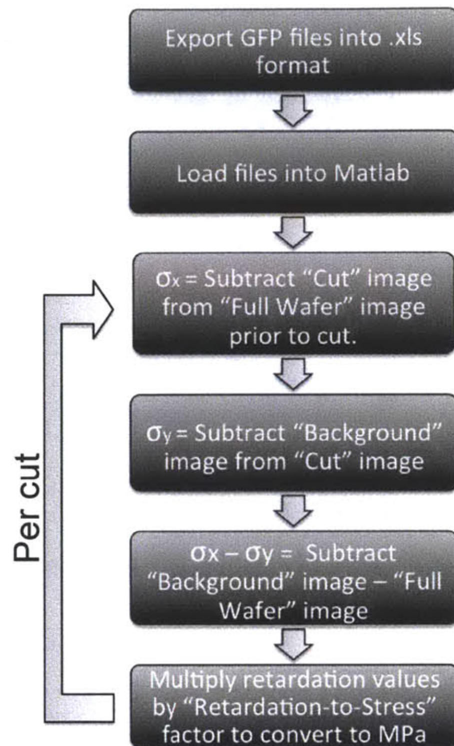


**Figure 3.6 - Process diagram of the analysis procedure to decouple stress components**

# 3.6 External Validation Techniques

XRD analysis was performed on the quasi-mono sample, given its single crystal and known (100) grain orientation to validate the previously presented technique and procedure. The measurements were done at MIT'S CMSE facilities, in a Rigaku SmartLab® high-resolution diffractometer, as seen in Figure 3.7. Details of the experimental and analysis procedure are presented elsewhere [53].

The quasi-mono diffraction peaks measured were for the (400), (440), and (404) planes. Following Equation 3.4, we input the lattice parameter value "d" obtained from XRD, and solve for lattice distances "a", "b", and "c", corresponding to a cubic lattice.

$$d_{hkl}^{-1} = \sqrt{\left(\frac{h}{a}\right)^2 + \left(\frac{k}{b}\right)^2 + \left(\frac{l}{c}\right)^2} \tag{3.4}$$

From these lattice distances, the strain can be resolved onto a particular direction and subsequently calculated. The strain calculation is done by taking the difference in values from the measured lattice distance ("*a*", "*b*", or "*c*") from $a_o$ = 5.431 Å, divided by $a_o$, as shown in Equations 3.5-3.7.

$$\varepsilon_a = \frac{a - a_o}{a_o} \tag{3.5}$$

$$\varepsilon_b = \frac{b - a_o}{a_o} \tag{3.6}$$

$$\varepsilon_c = \frac{c - a_o}{a_o} \tag{3.7}$$

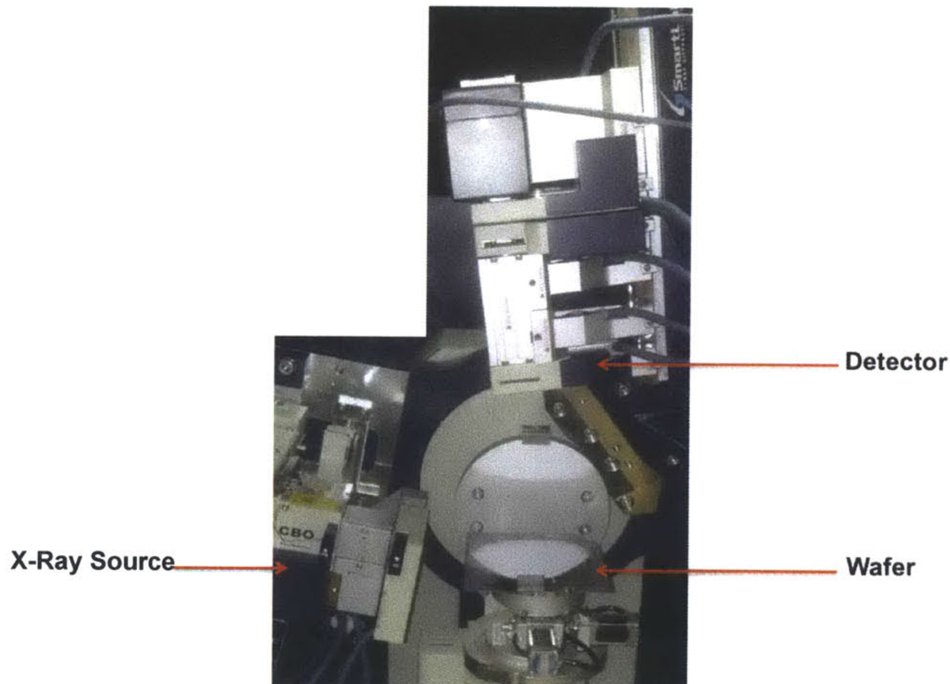


**Figure 3.7 – Rigaku SmartLab® setup with wafer placed in stage for peak diffraction analysis**

CHAPTER

# 4

# RESIDUAL STRESS EXPERIMENTAL RESULTS

This chapter presents the results obtained from sample preparation, and IBI with the continuous sectioning method. XRD strain measurement values are also presented for comparison.

## 4.1 Sample Preparation

### 4.1.1 Surface Smoothing

The mechanical polishing approach to planarize the wafer surfaces proved to be unsuccessful when tested on full size wafers. Cracks observed were presumably due to capillary forces coming from the pad-water-wafer interface. These forces are thought to have acted on the thin, polished surfaces upon the liftoff process and concentrated on regions of the wafer that lacked wax support on the mounting side. The wax-less regions consisting of air voids formed the equivalent to several small clamped cantilever beams prone to fracture with the exerted forces.

CMP, however, successfully planarized the surface resulting in wafer faces polished in similar degree to String Ribbon and Dendritic Web, as seen in Figure 4.1. The CMP technique resulted in a polished area forming a concentric circle within the wafer. This effect is due to the lack of translation (only rotation) from the pad during the polishing procedure. The approximated polished diameter for the mc-Si sample was of 13 cm, and of 10 cm for the quasi-mono wafer.

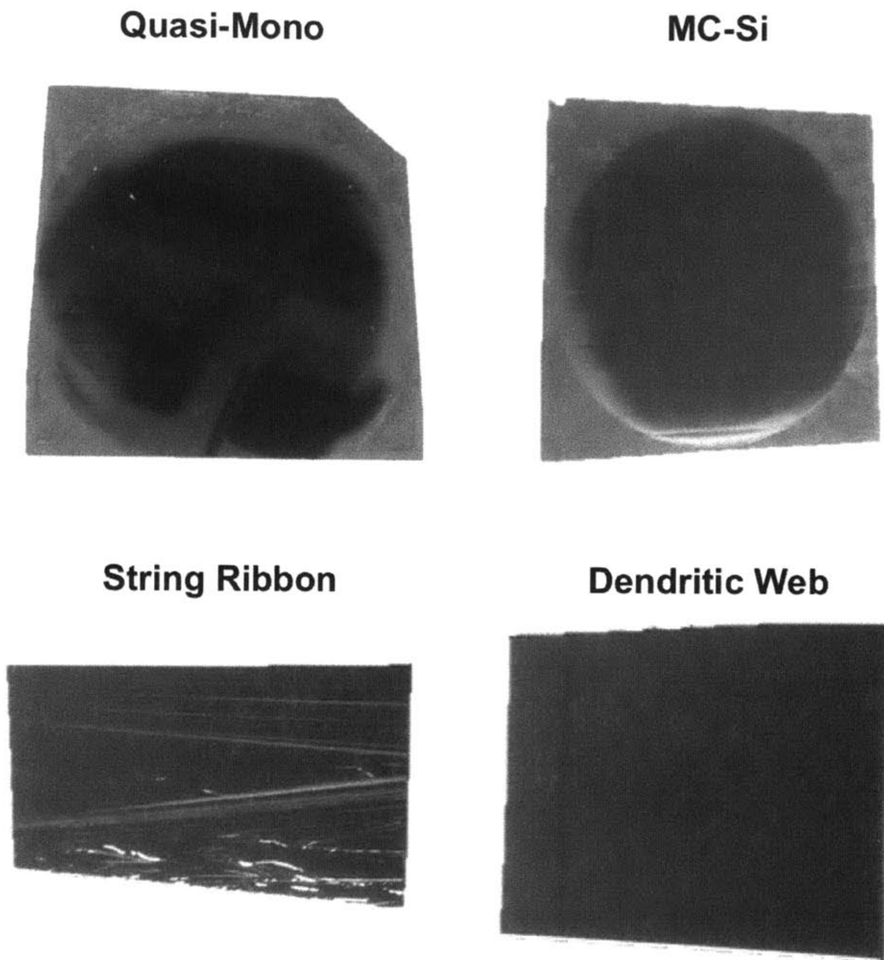


**Figure 4.1 - CMP images of Quasi-Mono and MC-Si, and As-grown String Ribbon and Dendritic Web**

**[Scale differs per image]**

### 4.1.2 Surface Cutting

Figure 4.2 shows the end result of laser-cutting the samples. The polished area of a wafer's front side varied slightly from the polished area of the wafer's back side due to wafer positioning during CMP. This offset resulted in areas within a circle that did not transmit any light, rendering unsuitable for IBI analysis. Therefore, the amount of cuts performed on each wafer does not necessarily represent the amount of lines from which useful information could be extracted, as it will be presented next.

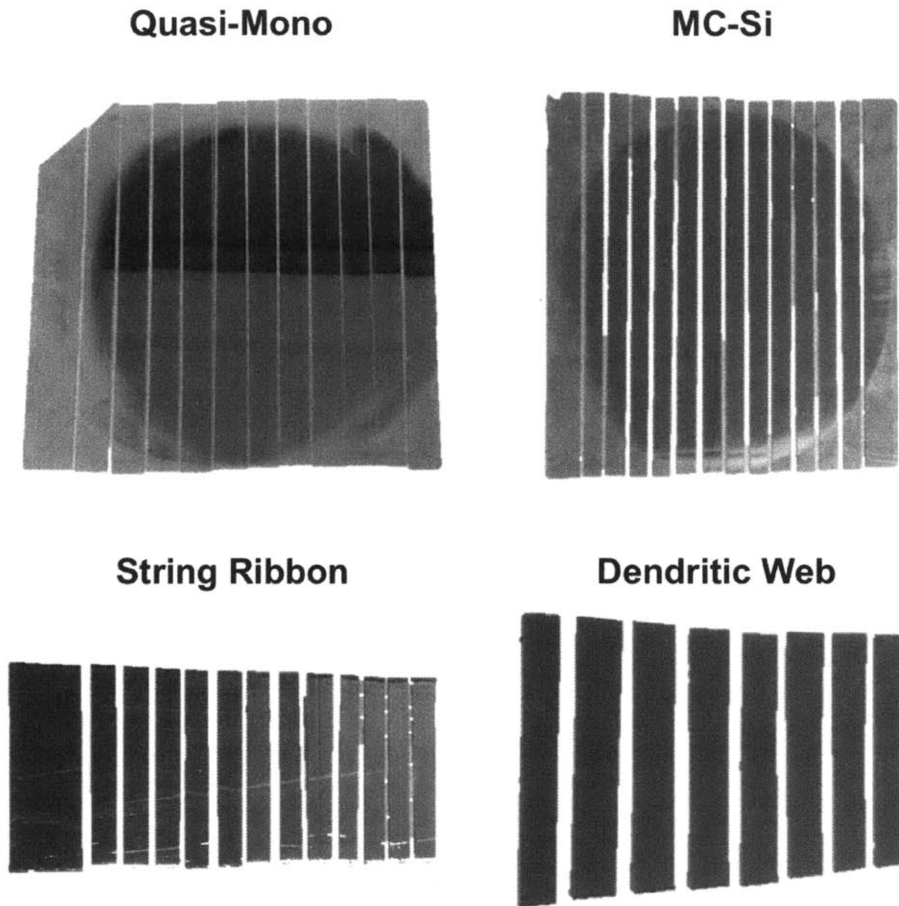


**Figure 4.2 - Quasi-Mono, MC-Si, String Ribbon, and Dendritic Web wafers after being cut**
**[Dendritic Web sample shown at an angle] [Scale differs per image]**

# 4.2 IBI Residual Stress Results

The effect of inclusions and line defects is automatically excluded from the residual stress analysis given the short characteristic length of stress, rendering these micro-defects stress signature's virtually fixed in space after the cut. Any differential imaging, therefore, results in a net-zero contribution from micro-defects, only elucidating the contribution from the relaxation of residual stress upon freeing of a surface.

### 4.2.1 Dendritic Web

Figure 4.3a shows the infrared transmission image of the Dendritic Web sample, as seen in the Stress Photonics® Software. In Fig 4.3a dark color corresponds to low light transmission levels, and bright color corresponds to high light transmission levels. The red-dash lines in Fig. 4.3a highlight the regions where the sample was sequentially cut vertically. Figure 4.3b shows the image representing $\sigma_x$-$\sigma_y$ values before being cut. There is a subtle crosshatched pattern that can be seen, and it is due to the dislocations formed during this growth process at 45° from the abscissa. Figure 4.3c shows the contribution due to the cutting of Line 1; the 'before cut' image is subtracted from the 'after cut' image and the $\sigma_x$ contribution is then decoupled at the edge. Lastly, Figure 4.3d shows the effect of Line 1 on the signal that leads to obtaining $\sigma_y$.

The retardation values at the immediate edge are converted to stress values and plotted as shown on Figure 4.4. In these plots, the black line represents $\sigma_x$-$\sigma_y$, which is the value extracted by the conventional method without cleaving, and on the line of interest. The red and blue lines represent the deconvolution of the black line ($\sigma_x$-$\sigma_y$) into $\sigma_y$, and $\sigma_x$, respectively.

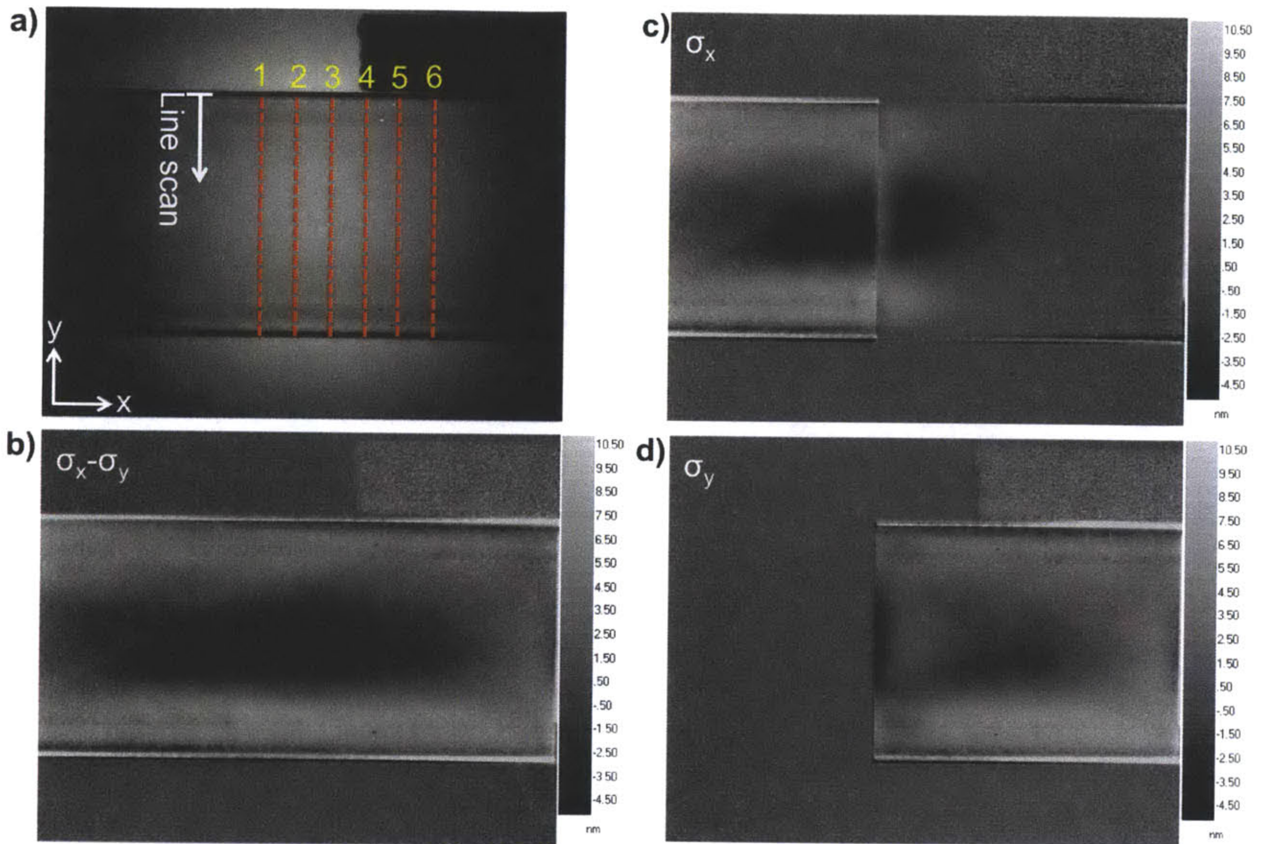


**Figure 4.3 - a) Infrared transmission image of a Dendritic Web sample with dashed lines representing regions where stress distribution was analyzed via the continuous sectioning method. Lines are numbered 1-6. b) $\sigma_x$-$\sigma_y$ image of the sample prior to cut. c) Image of cut wafer through line 1 subtracted from full wafer to obtain $\sigma_x$. d) Image of cut wafer through line 1 with background subtracted to obtain $\sigma_y$**

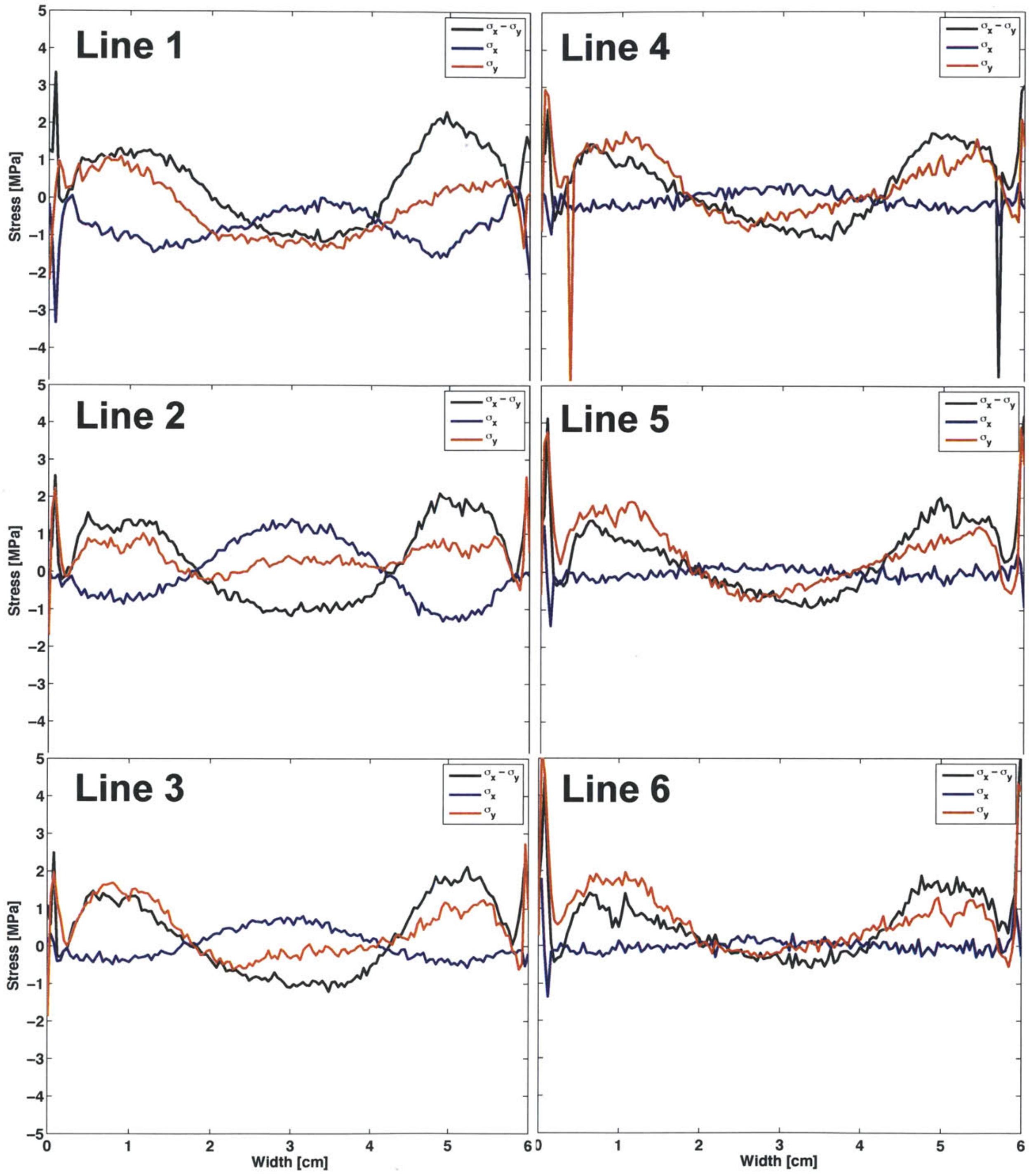


**Figure 4.4 - Line plots showing the stress distribution profile in Dendritic Web silicon sample: $\sigma_x$-$\sigma_y$ (black), $\sigma_x$ (blue), and $\sigma_y$ (red) at line cuts 1-6 highlighted in Fig. 4.3a**

Normal stress values in the x direction, or $\sigma_x$, reach -3 MPa close to the edges and 1.4 MPa at the center, as is the case in line 1, and 2, respectively. Normal stress values in the y direction, or $\sigma_y$, are close to 3.7 MPa near the edge, and 1.8 and -0.7 MPa away from it, as seen in line 5 in Figure 4.4.

### 4.2.2 String Ribbon

Similarly, Figure 4.5a shows the infrared transmission image of the String Ribbon sample. In Fig 4.5a dark color corresponds to low light transmission levels, and bright color corresponds to high light transmission levels. The repeatable vertical ripple-like features are a characteristic surface effect from this ribbon growth process. The dark elongated lines running parallel to each other correspond to twin bands that alter the surface planarity and tend to come out of plane.

Figure 4.5a contains eight dashed lines that correspond to the regions where the sample was sequentially cut vertically. Figure 4.5b shows the image representing $\sigma_x$-$\sigma_y$ values before being cut. Figure 4.5c shows the contribution due to the cutting of Line 4; the 'before cut' image is subtracted from the 'after cut' image and the $\sigma_x$ contribution is then decoupled at the edge. Figure 4.5d shows the effect of Line 4 on the signal that leads to obtaining $\sigma_y$.

The retardation values at the immediate edge are converted to stress values and plotted as shown on Figure 4.6. The black lines in these plots represent $\sigma_x$-$\sigma_y$, which is the value extracted by the conventional method without cleaving, on the line of interest. The red and blue lines represent the deconvolution of the black line ($\sigma_x$-$\sigma_y$) into $\sigma_y$, and $\sigma_x$, respectively.

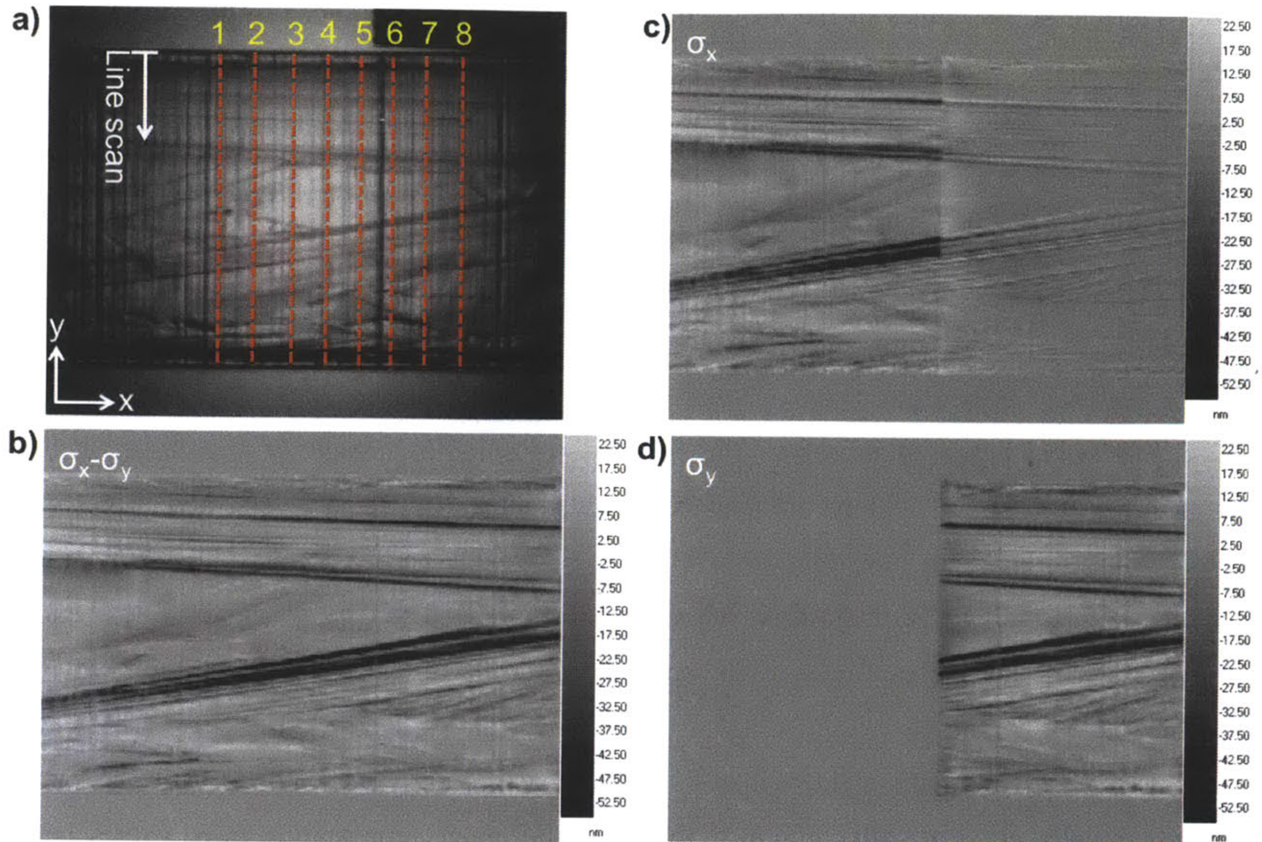


**Figure 4.5 a) Infrared transmission image of a String Ribbon sample with dashed lines representing regions where stress distribution was analyzed via the continuous sectioning method. Lines are numbered 1-8. b) $\sigma_x$-$\sigma_y$ image of the sample prior to cut. c) Image of cut wafer through Line 4 subtracted from full wafer to obtain $\sigma_x$. d) Image of cut wafer through Line 4 with background subtracted to obtain $\sigma_y$**

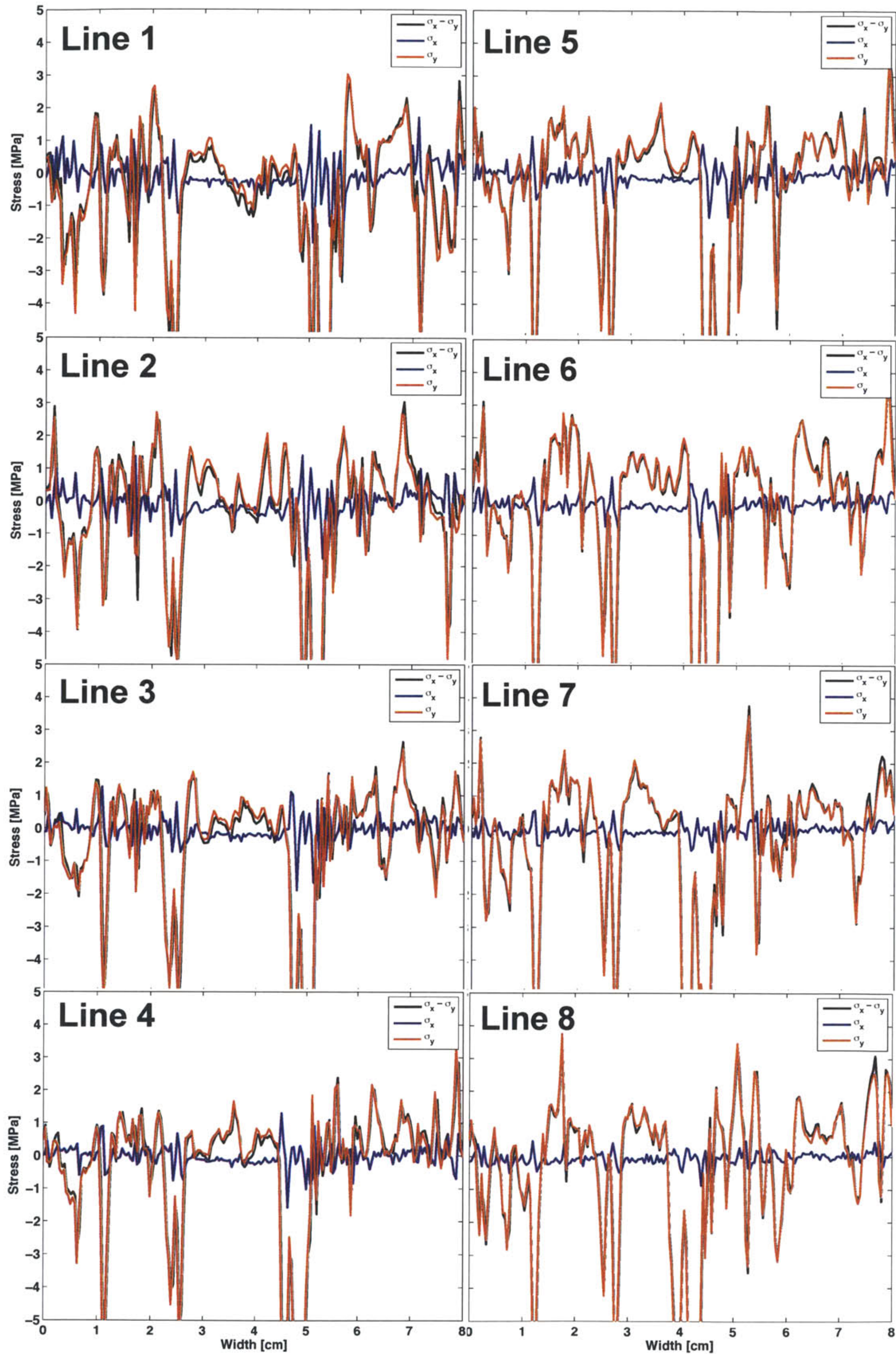


**Figure 4.6 - Line plots showing the stress distribution profile in String Ribbon silicon sample: $\sigma_x$-$\sigma_y$ (black), $\sigma_x$ (blue), and $\sigma_y$ (red) at line cuts 1-8 highlighted in Fig. 4.5a**

Normal stress values in the x direction ($\sigma_x$) tend to be relatively small, except for some regions that are 1.78 MPa, and -1.75 MPa, as seen in line 1 of Figure 4.6. Normal stress values in the y direction ($\sigma_y$) are close to 3.4 and -8.5 MPa, as obtained from line 8 in Figure 4.6.

### 4.2.3 Multicrystalline Silicon

As before, Figure 4.7a shows the infrared transmission image of the mc-Si sample where a dark color corresponds to low light transmission levels, and bright color corresponds to high light transmission levels. As opposed to the previous case with String Ribbon, the sample structure is sufficiently planar so no features can be readily seen in transmission mode.

Figure 4.7a contains eight dashed lines that correspond to the regions where the sample was sequentially cut vertically. Figure 4.5b shows the image representing $\sigma_x$-$\sigma_y$ values before being cut. It is important to note that there is a distinguishable introduction of stress signal arising from defects in this $\sigma_x$-$\sigma_y$ image in comparison to the pure infrared transmission image. Figure 4.7c shows the contribution due to the cutting of Line 4; the 'before cut' image is subtracted from the 'after cut' image and the $\sigma_x$ contribution is then decoupled. Lastly, Figure 4.7d shows the effect of Line 4 on the signal that leads to obtaining $\sigma_y$.

The retardation values at the immediate edge are converted to stress values and plotted as shown on Figure 4.8. The black lines in these plots represent $\sigma_x$-$\sigma_y$, which is the value extracted by the conventional method without cleaving, on the line of interest. The red and blue lines represent the deconvolution of the black line ($\sigma_x$-$\sigma_y$) into $\sigma_y$, and $\sigma_x$, respectively.

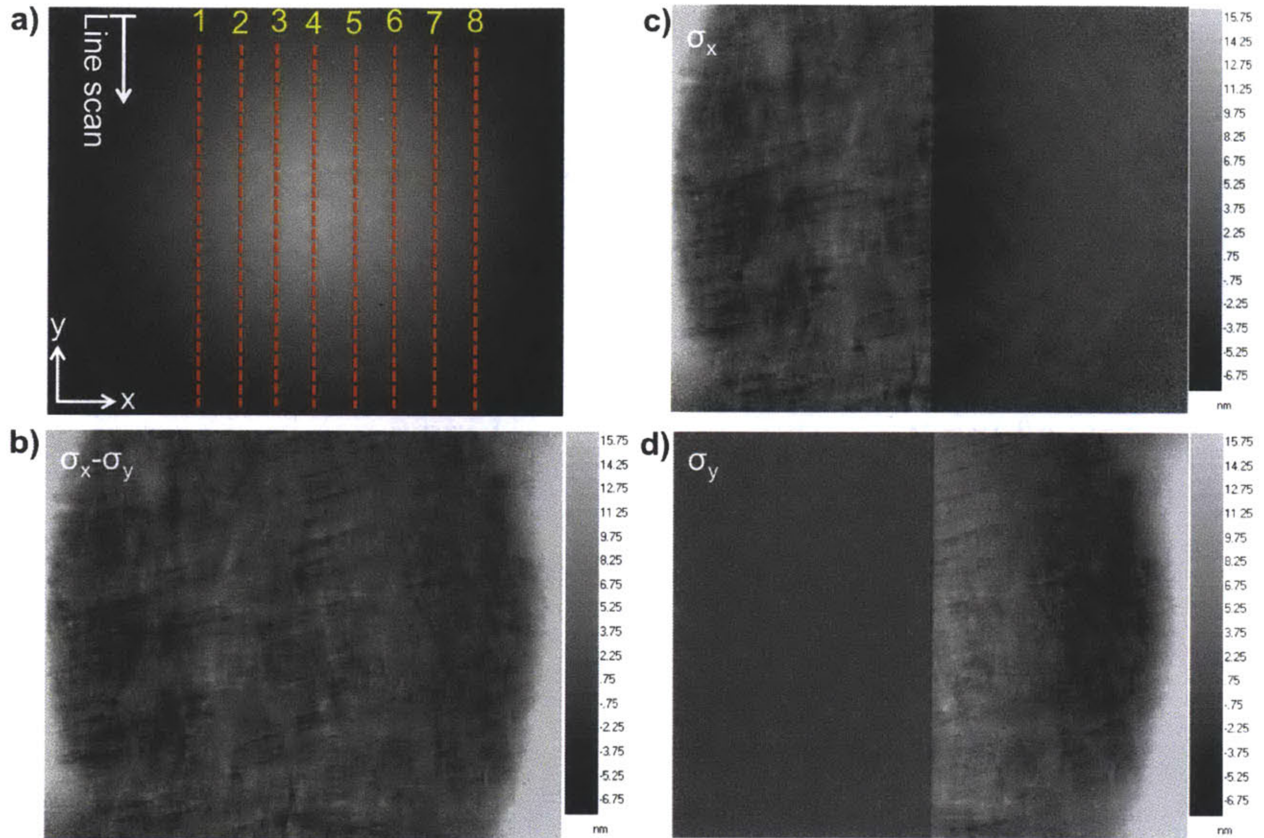


**Figure 4.7 a) Infrared transmission image of a mc-Si sample with dashed lines representing regions where stress distribution was analyzed via the continuous sectioning method. Lines are numbered 1-8. b) $\sigma_x$-$\sigma_y$ image of the sample prior to cut. c) Image of cut wafer through Line 4 subtracted from full wafer to obtain $\sigma_x$. d) Image of cut wafer through Line 4 with background subtracted to obtain $\sigma_y$**

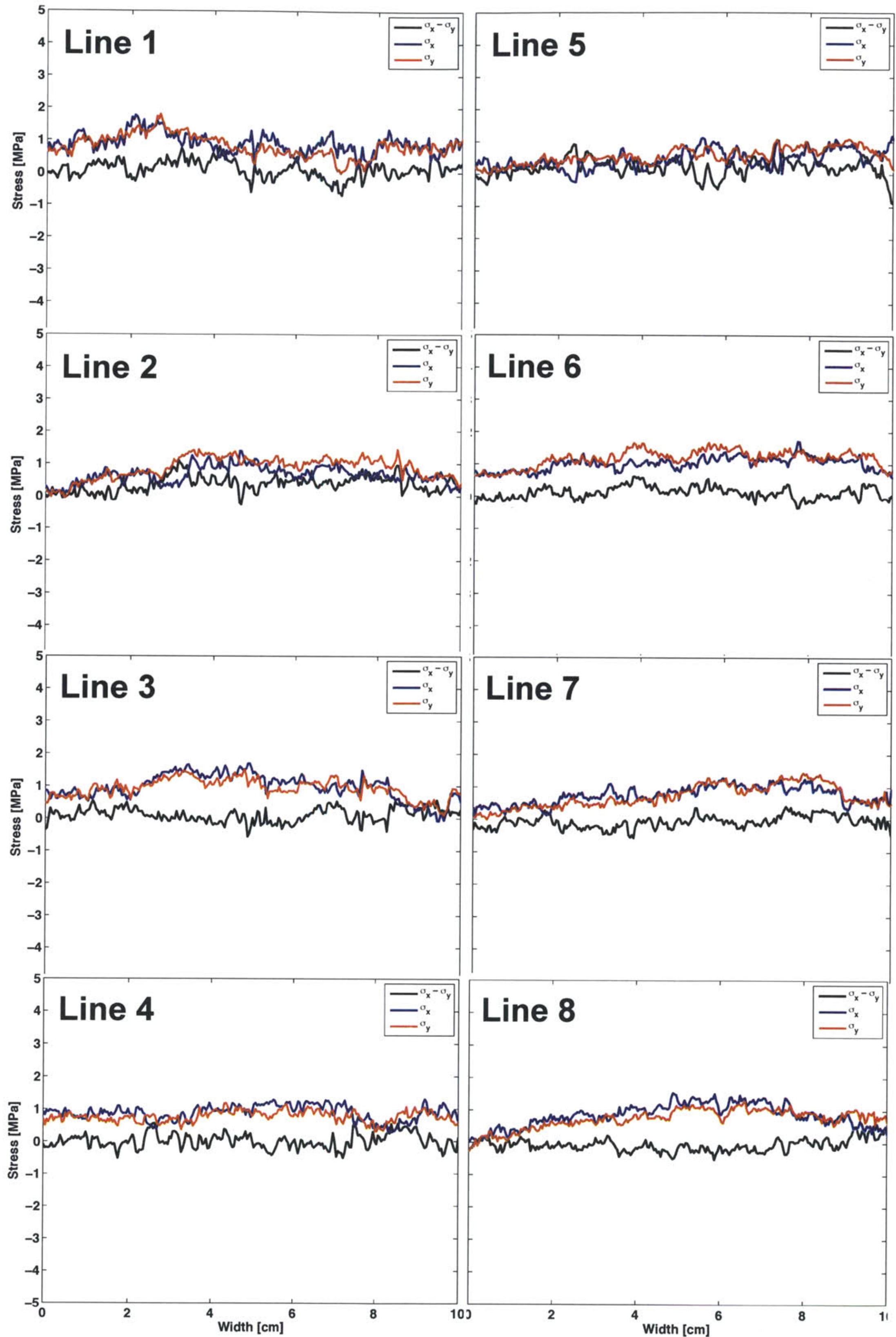


**Figure 4.8 - Line plots showing the stress distribution profile in a mc-Si sample: $\sigma_x$-$\sigma_y$ (black), $\sigma_x$ (blue), and $\sigma_y$ (red) at line cuts 1-8 highlighted in Fig. 4.7a**

Normal stress values in the x direction ($\sigma_x$) can vary between1.28 or 0.37 MPa at the center, as is the case in line 4. Normal stress values in the y direction ($\sigma_y$) can reach 1.67 MPa, as seen in line 6 in Figure 4.8.

### 4.2.4 Quasi-Mono

Lastly, Figure 4.9a shows the infrared transmission image of the quasi-mono sample, where dark color corresponds to low light transmission levels, and bright color corresponds to high light transmission levels. Similar to the case of mc-Si, the planarization doesn't allow any features in the infrared image to be observed.

Eight dashed lines that correspond to the regions where the sample was sequentially cut vertically are shown in Figure 4.9a. Figure 4.9b shows the image representing $\sigma_x$-$\sigma_y$ values before being cut. Figure 4.9c shows the contribution due to the cutting of Line 4; the 'before cut' image is subtracted from the 'after cut' image and the $\sigma_x$ contribution is then decoupled at the edge. On this same line, the effect on the signal that leads to obtaining $\sigma_y$ is shown in Figure 4.9d.

The retardation values at the immediate edge are converted to stress values and plotted as shown in Figure 4.10. The black lines in these plots represent $\sigma_x$-$\sigma_y$, which is the value extracted by the conventional method without cleaving, on the line of interest. The red and blue lines represent the deconvolution of the black line ($\sigma_x$-$\sigma_y$) into $\sigma_y$, and $\sigma_x$, respectively.

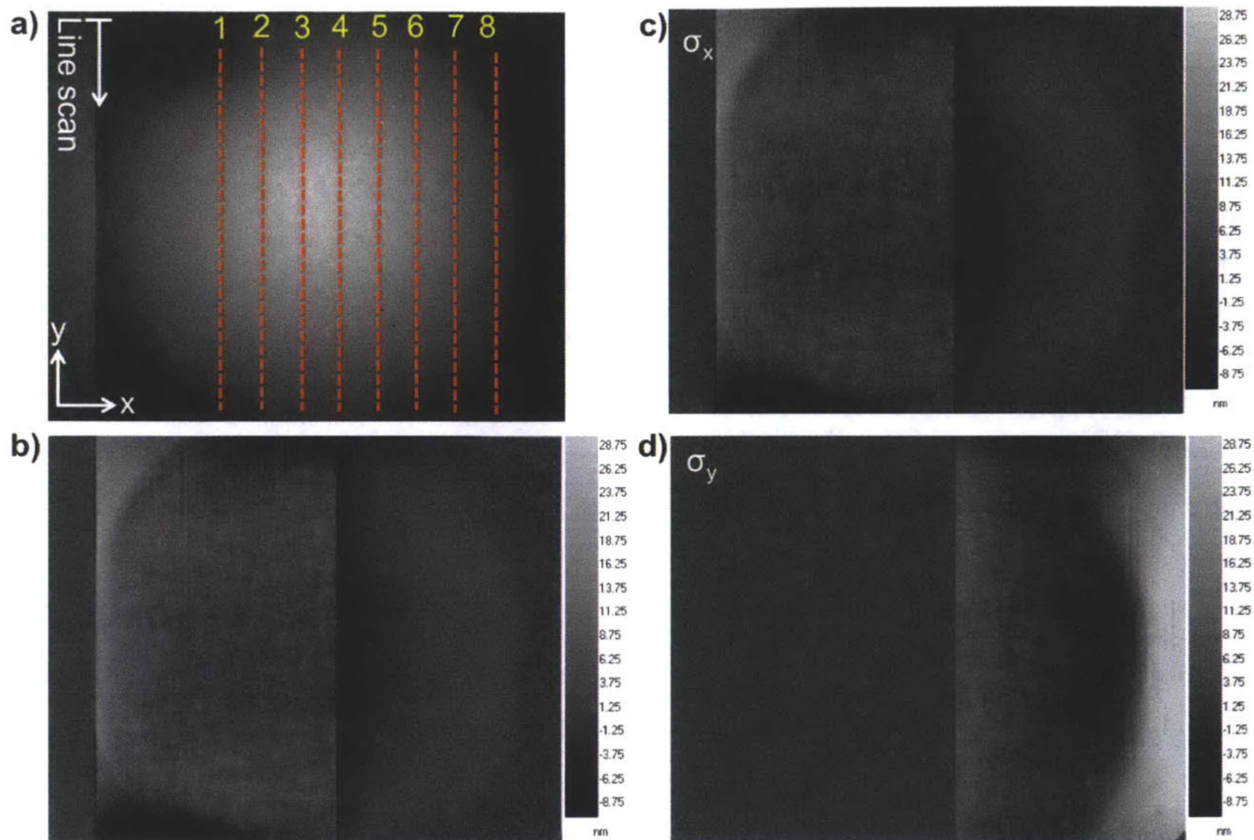


**Figure 4.9 a) Infrared transmission image of a quasi-mono sample with dashed lines representing regions where stress distribution was analyzed via the continuous sectioning method. Lines are numbered 1-8. b) $\sigma_x$-$\sigma_y$ image of the sample prior to cut. c) Image of cut wafer through Line 4 subtracted from full wafer to obtain $\sigma_x$. d) Image of cut wafer through Line 4 with background subtracted to obtain $\sigma_y$**

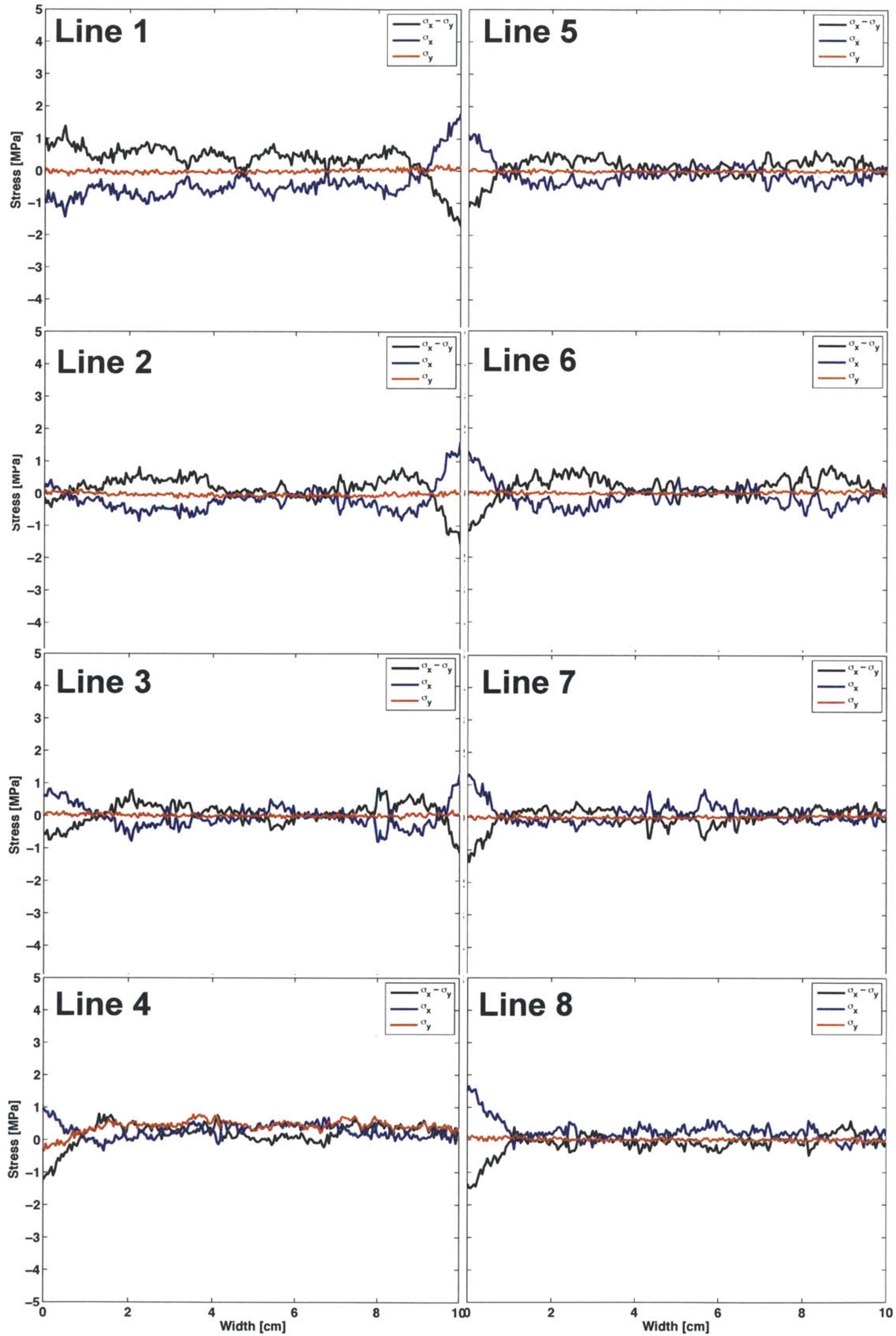


**Figure 4.10 - Line plots showing the stress distribution profile in a quasi-mono Si sample: $\sigma_x$-$\sigma_y$ (black), $\sigma_x$ (blue), and $\sigma_y$ (red) at line cuts 1-8 highlighted in Fig. 4.9a**

Normal stress values in the x direction, or $\sigma_x$, reach 0.88 MPa at the center, as is the case in line 6. Normal stress values in the y direction, or $\sigma_y$, are close to 0.78 MPa, as seen in line 4 in Figure 4.10.

## 4.3 XRD Residual Stress Results

Residual strain measurements on the center of the quasi-mono sample, with a probing area of 10 mm wide × 5 mm long were conducted with XRD. The values shown on Table 2.1 were obtained. Assuming a Young's Modulus of $E$ = 130 GPa, corresponding to a (100) orientation, the stress values for $\sigma_x$ and $\sigma_y$ are calculated to be 53.7 and 59.2 MPa, respectively.

**Table A.1 - XRD residual strain and stress calculations for quasi-mono Si sample**

| $a_0$ (Å) | | $a_z$ (Å) | $a_x$ (Å) | $a_y$ (Å) |
|---|---|---|---|---|
| 5.430896 | | 5.42972 | 5.43314 | 5.43337 |
| | Difference = | -0.0217% | 0.0413% | 0.0456% |
| Stress | [Pa] | -28150051.1 | 53714893.4 | 59220430.6 |
| Stress | [Gpa] | -0.02815005 | 0.05371489 | 0.05922043 |
| Stress | [MPa] | -28.150 | 53.714 | 59.220 |

CHAPTER

# 5

# DISCUSSION

The hypothesis of the capability of measuring residual stress by IBI was tested on four different samples. The residual stress distribution was measured with the IBI system and decoupled into its normal stress components by cutting the sample multiple times. An XRD strain measurement method was used to compare values obtained with the IBI stress values. The significance of the results is presented herein.

## 5.1 Residual Stress in Silicon Materials

### 5.1.1 Dendritic Web

The stress values observed in the Dendritic Web stress plots follow the distribution trend previously reported in ref. [44], with a tension-compression-tension profile in the y-direction of the sample. This stress distribution arises from the lateral and longitudinal temperature profile, ribbon width, and thickness [50].

Previously reported stress values range from 0.10 MPa to 4 MPa via the split width method [50]. In this contribution we found values lying between 1.5 and ~4 MPa. From the stress plots produced in this work, we observe that the values reported herein are consistent within the aforementioned reported stress values, thus corroborating the hypothesis test and results.

It is interesting to note that in this experiment, the decoupled stress profiles are indeed very similar to those from ref. [44], however, slightly lower. We believe that this difference is attributed to a difference in growth processing between the samples analyzed in each study.

The stress distribution as a function of cut line, $\sigma_x$ and $\sigma_y$, the profile shape does not vary much as the line cut progresses towards the right end of the sample. This minimal variation in profile can be interpreted as a low difference in growth characteristics between contiguous segments of the same wafer piece.

The edge stabilization process in the Dendritic Web growth is completed by propagating dendrites into the sample while locally supercooling the melt at the edge [12]. This local supercooling leads to a thicker region. The high residual stress peaks at the edges observed on Figure 4.4, correspond to the location where supercooling begins, and where the sample is thicker as well. The decoupling of contributions to the retardation values arising from thickness variation and from residual stress was not explored in this study.

### 5.1.2 String Ribbon

The String Ribbon sample, in contrast with the other evaluated samples, shows a visible thickness variation throughout the sample's length, evident by the vertical lines in Figure 4.5a. This continuous thickness variation is the result of the heat flux balance at the interface, which takes into account the pulling speed and its effect on the local melt temperature profile [54].

Another important feature observed is the presence of twin bands growing parallel or at an angle with respect to the pulling direction (x-axis, in Figure 4.5). The presence of twin bands alters the surface flatness and impacts light propagation, as seen in the infrared transmission image from Figure 4.5a. When comparing the stress values from Figure 4.6, we see that a substantial increase or decrease in retardation values correspond to the location of twin bands. Therefore, the possibility of having measured stress values with more than -8 MPa could be thought to be due to the surface roughness affecting light conditions.

On the other hand, studies on edge-defined film-fed growth (EFG), a ribbon-growth technology similar to String Ribbon [55, 56] have measured stress in twinned regions via stress-induced double diffraction and Raman spectroscopy [57]. These measurements concluded that

the silicon-carbon lattice distance in the twinned-region was reduced by 15% in comparison to the silicon-silicon lattice distances elsewhere, hence leading to localized stress values of 20 MPa and above. Other studies in mc-Si twinned regions have reported values in the order of 10 MPa [58]. We find our results of having highly stressed regions in twinned areas to be in agreement with such literature reports. Although our reported values are lower, this can be explained by the higher spatial resolution of the techniques used in ref. [57], and by the fact that the sample used herein is from a different growth method [57, 58].

From the stress profile plots in Figure 4.6, it is evident that the majority of the measured stress in this sample arises from the twin band regions, and in the y-axis direction. The relaxation, thus, seems negligible and the strain is thought to remain locked by the twin bands.

### 5.1.3 Mc-Si

As previously mentioned, the infrared transmission image in Figure 4.7a shows no features due to surface variations, which translates into a higher certainty on the origin of the stress values obtained.

For most of the regions analyzed in this sample, $\sigma_x$ and $\sigma_y$ values are similar both in distribution and in magnitude (~0.8-1.8 MPa). These values are consistent with other variations of IBI measurements previously reported, giving an average value of 1.31 MPa for the chemically polished mc-Si wafers [33], and the similar low stress values (much lower than 10 MPa) reported in mc-Si regions [58].

Although the wafer position on the ingot is not known, we posit, given its symmetric profile both in the y- and x-directions as seen in Figure 4.8, that this sample might have come from a position in the center of the ingot, which is the final place to cool down given its equidistance to a heat-dissipating boundary [59]. This equidistance could explain the symmetric stress profile. Moreover, the residual stress value obtained herein, is approximate to the simulated theoretical values of 2.8 MPa, for said position at similar heights from which this wafer was obtained [30].

### 5.1.4 Quasi-mono

From Figure 4.10, we can conclude that the quasi-mono sample contained the least amount of residual stress measured. Only contributions from $\sigma_x$ were for almost all of the cuts.

Being an ingot casting method similar to mc-Si, one could expect stress values to be similar. However, the lower residual stress values in this growth method can be explained by the lack of multiple grains, their boundaries interaction, and geometrically needed dislocations originating from a confined multicrystalline system subjected to a loading [60]. These grain interactions, as shown previously in Figure 1.1, can raise the overall stress state of a multicrystalline sample. Therefore, although the same geometrical (and potentially cooling) conditions exist, the nature of the crystal structure (*i.e.*, single-crystal) leads to a reduced amount of residual stress.

In all of the quasi-mono plots showing the residual stress profile, the signal ($\sigma_x$-$\sigma_y$) either starts or ends lower than the rest of the retardation signal probed along the sample's width. This effect can be understood by looking at the polished pattern of the sample: regions that were poorly polished, located outside the finely polished area, tend to absorb more light. This uneven absorption leads to an unusual retardation pattern, which corresponds to the low signal.

### 5.1.5 Comparison

A summary of the stress profiles obtained, and a set of representative line scans from each sample is shown in Figure 5.1.

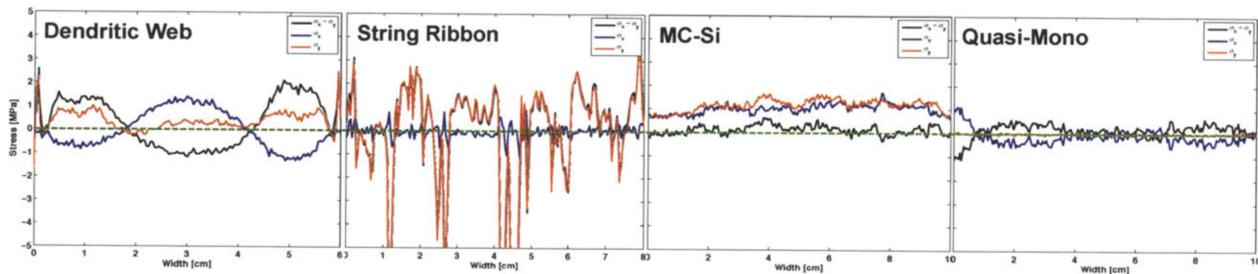


**Figure 5.1 – Comparison of representative line scans from the four different Si samples. Lines correspond to $\sigma_x$-$\sigma_y$ (black), $\sigma_x$ (blue), and $\sigma_y$ (red). Green dashed line represents zero stress.**

It is evident from this figure that the sample with the highest residual stress is String Ribbon given its high density of twin bands. The next sample with the most amount of residual stress is Dendritic Web with its sinusoidal stress distribution profile, followed by the symmetric stress profile of mc-Si, and lastly the lowly stressed quasi-mono.

### 5.1.6 XRD Results

XRD measurements resulted in high stress values in quasi-mono (~50 MPa), in comparison to the relatively small values obtained from IBI (~1 MPa). However, there are some inconsistencies in the XRD values: After taking a ratio of strain values in perpendicular directions (*i.e.*, Poisson's ratio, ν), the value obtained for the quasi-mono sample was of 0.54, which is almost twice as ν=0.28, the Poisson's ratio for the 100 orientation in Si [61].

This discrepancy indicates a potential error in the data acquisition. Potential sources of error could be easily introduced during the setup calibration. A 1/1000$^{th}$ discrepancy in calibration can propagate to substantial differences in expected results, including what we observed as a factor of two difference in ν.

Furthermore, the possibility of having probed intragranular stresses on top of residual stresses, as shown in Figure 1.1, should not be discarded. Interestingly, however, is the fact that the signs of the stress tensor were measured to be positive (for tensile), consistent with the expected and measured values from the IBI technique.

Proper XRD calibration measures, as well as further measurements on more samples with this technique need to be taken for XRD to be considered in a reliable, accessible, non-spatially resolved approach for corroborating IBI stress results.

CHAPTER

# 6

# FUTURE WORK

While IBI and sectioning was demonstrated to provide useful information regarding normal stress components of residual stress in silicon, there is still potential for improvement in different steps of the acquisition and analysis procedure.

### 6.1.1 Refinement of Assumptions

One of the crucial assumptions of this work is that the stress component parallel to the cut remains the same after the cut, and hence by an image difference (before and after cutting), the contribution of the perpendicular stress component can be deduced. This assumption, however, ignores some details that can lead to an offset of the final stress value. The description of the mechanical behavior is as follows:

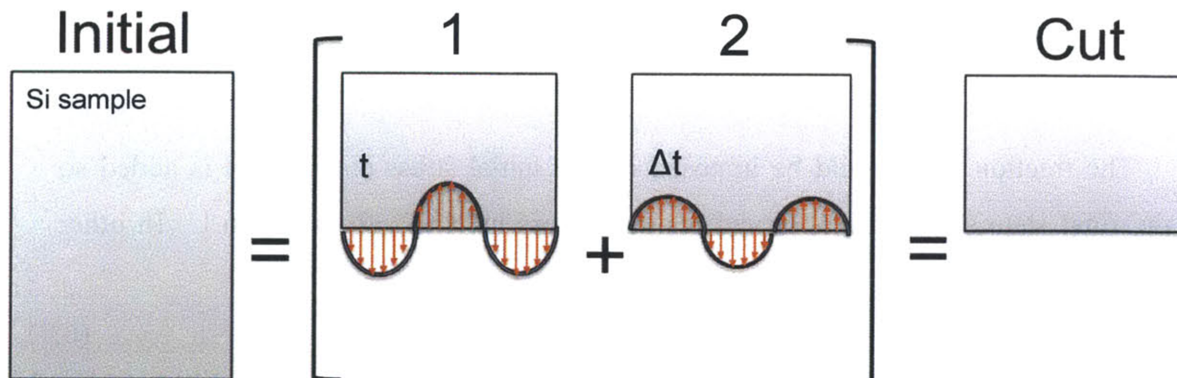


**Figure 6.1 - breaking the initial stress state into the traction originally present (t), and the traction difference $\Delta t$ (*i.e.*, residual) imposed to lead to the final cut value**

Decoupling the components of the "Initial" stress state, the following equations are obtained

$$\sigma_{ij}{}^{initial} \qquad (6.1)$$

$$\sigma_{yy}{}^{initial}$$

$$\sigma_{xx}{}^{initial}$$

and from the stress-optic law, the signal obtained is

$$Birefringence_{initial} = \sigma_{xx}{}^{initial} - \sigma_{yy}{}^{initial} \qquad (6.2)$$

Going from the "Initial" state to the final "Cut" state, the process can be broken down into two intermediate states, as seen in Figure 6.1. The broken piece initially contains the entire stress distribution as if no cleaving was done (labeled #1). Then by adding another step (labeled #2), which is the counter tractions, or the residual stress complementary in negative direction that when added to state #1, leads to the final value of "Cut".

From state 1, representing the original traction present in the sample, the following equations are found

$$\sigma^{\#1}{}_{ij} = \sigma_{ij}{}^{initial} \qquad (6.3)$$

$$\sigma^{\#1}{}_{yy} = \sigma_{yy}{}^{initial}$$

$$\sigma^{\#1}{}_{xx} = \sigma_{xx}{}^{initial}$$

The traction that should be imposed on the initial stress distribution is added so that the final state shows the observed residual stress in "Cut", from Fig. 6.1. In other words,

$$\sigma^{\#2}{}_{ij} = \sigma_{ij}{}^{\Delta t} \qquad (6.4)$$

$$\sigma^{\#2}{}_{yy}|_{y=0\ (at\ the\ cut\ origin)} = -\sigma^{\#1}{}_{yy(x)} = -\sigma_{yy(x)}{}^{initial}$$

$$\sigma^{\#2}{}_{xx} = ?$$

The first balance comes from shear equilibrium at the cut interface. The stress component in the x-direction cannot be directly obtained (by balance), and equilibrium equations and stress strain relations are required. This impacts the final stress value calculation on "Cut".

$$\sigma^{Cut}{}_{ij} = \sigma^{\#1}{}_{ij} + \sigma^{\#2}{}_{ij} \tag{6.5}$$
$$\sigma^{Cut}{}_{yy} = \sigma_{yy}{}^{\#1} + \sigma_{yy}{}^{\#2}$$

The second equation in (6.5) corroborates the second equation in (6.4), stating the boundary conditions of $\sigma^{\#2}{}_{yy}|_{y=0} = 0$ at the cut leaves the equality of $-\sigma^{\#1}{}_{yy(x)} = -\sigma_{yy(x)}{}^{initial}$ previously expressed.

In the x-axis, the equations found are

$$\sigma^{Cut}{}_{xx} = \sigma^{\#1}{}_{xx} + \sigma^{\#2}{}_{xx} \tag{6.6}$$
$$= \sigma^{initial}{}_{xx} + \sigma_{xx}{}^{\#2}$$

When translating into the obtained retardation value obtained from the stress-optic law, it is noted that

$$Birefringence_{Cut} = \sigma_{xx}{}^{Cut} - \sigma_{yy}{}^{Cut} \tag{6.7}$$

The value of $\sigma_{yy}{}^{Cut}$ in this case is zero, and so by subtracting the two birefringence values (before cut - after cut), as it is done to decouple stress components, the relations obtained are

$$Birefringence_{Cut-initial} = \sigma^{Cut}{}_{xx} - (\sigma^{initial}{}_{xx} - \sigma^{initial}{}_{yy}) \tag{6.8}$$
$$Birefringence_{Cut-initial} = \sigma^{\#2}{}_{xx} + \sigma^{initial}{}_{yy}$$

Which carries the $\sigma^{\#2}{}_{xx}$ residue from before. For this case, the procedure can be either to neglect the $\sigma^{\#2}{}_{xx}$ component, as it was done in the current analysis, or introduce a dummy stress function that satisfies the final values that lead to the observed result.

### 6.1.2 Applied Load-to-Retardation Calibration

To minimize variation in the obtained values from IBI, a correction coefficient can be explored. To do this, an option is to impart a known loading condition to a sample, calculate the stress, and compare it against the retardation (and stress) values from the IBI technique.

As an aid for future studies, a four point bending device was machined to calibrate measurements by mechanically bending a wide variety of samples with different grain orientations, thicknesses, and dopants concentrations, as all of these variables are known to affect light transmission, and consequently, impact the final retardation value.

The constructed setup has a loading cell that is calibrated to show the applied load (in KgF). IBI stress values, calculated from Equation (3.1), can then be compared to the stress values originated from mechanical loading on four-point bending, shown in Equation (6.9).

$$\sigma_{bending} = \frac{3 * P * (L - L_i)}{2 * b * h^2} \tag{6.9}$$

Furthermore, to assess the impact on retardation values from the light variation over the camera's field of view, a silicon beam with a known applied load can be translated across different positions to be imaged by the camera. At all times the center region of the beam should give the same retardation values, otherwise, a correction based on the stage position should be implemented.

Images and further four point bending setup details are shown in Appendix B.

### 6.1.3 FEA Simulation of Alternative Method

An alternative method which avoids cutting through the entire sample's width is to make discrete cuts, and based on simulation, model the residual loads that would lead to the observed stress at the crack tip. This method is similar to the Contour method described in Section 1.6.

For this approach, initial finite element simulations were developed to serve as guidelines, as seen in Figure 6.2.

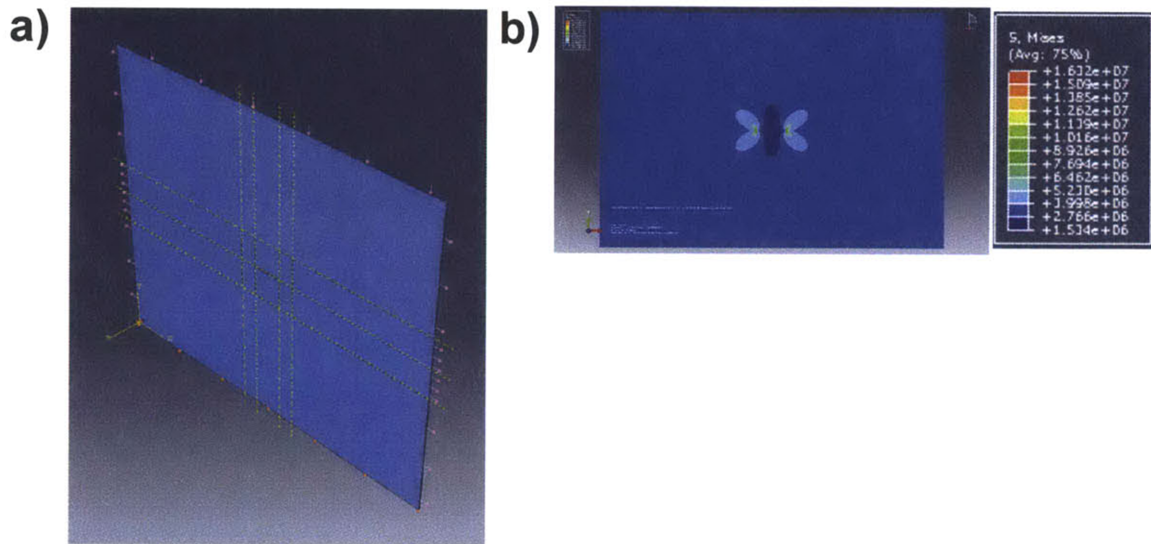


**Figure 6.2 - a) ABAQUS FEA model of Si Dendritic Web wafer with a through-crack in the center. b) Stress distribution upon external loading over the y- and x-axis**

Further studies could explore the deviation between the analytical, experimental, and FEA simulation from the cracks and determine what the residual stress distribution should be to match the experimental results. Figure 6.3 shows the comparison between simulation and analytical solution from the stress evolution away from a crack.

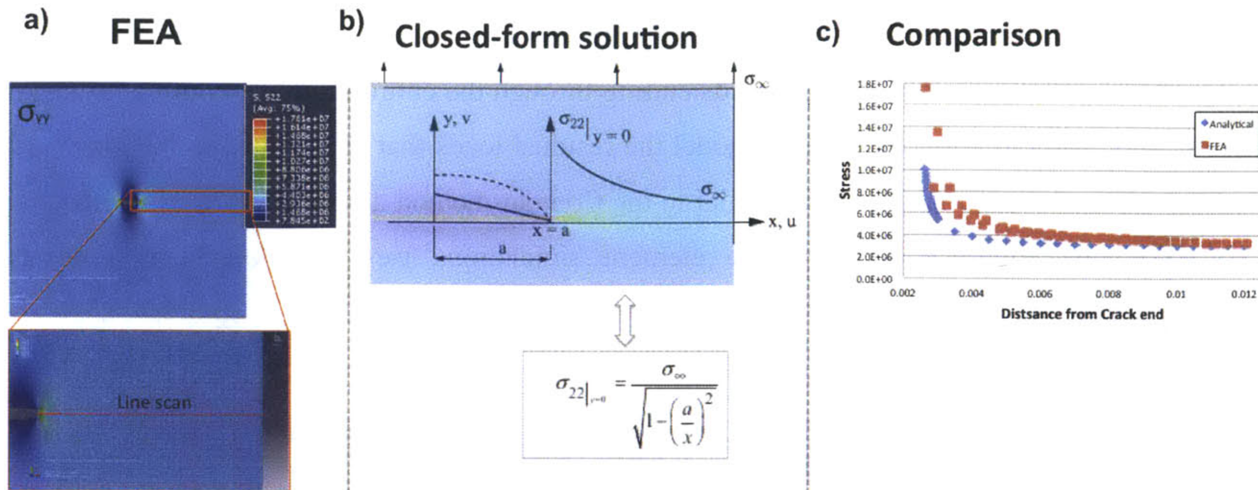


**Figure 6.3 - a) FEA simulation of a crack subjected to loading. b) Closed-form solution from the stress distribution away from a crack. c) Comparison of Analytical and FEA model**

Experimentally, an attempt to aid future work is shown in Figure 6.4, where a crack is introduced in a Dendritic Web sample and imaged via IBI. The After-Before image, which corrects for the background, leads to a visual match between IBI and FEA, opening the possibility of calculating the existing residual stress.

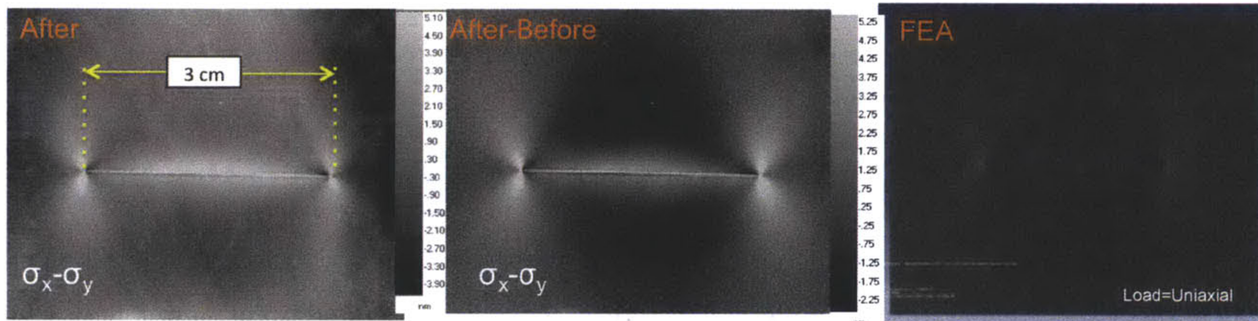


**Figure 6.4 - IBI image of a 3 cm crack introduced in IBI. A progression from an IBI image where no background correction is done, to one with correction is shown. An FEA simulation of the crack is shown to visually match the experimental stress distribution**

Furthermore, a theoretical approach has been reported by Vaidyanathan [62] to determine the amount of residual stress based upon measuring stress intensity factors (K) from crack tips. These potential approaches rely heavily on fracture mechanics expertise.

### 6.1.4 Software and Polarizer Manipulation

One of the limitations stated previously was a lack of control over the processing algorithm and the polarizer position. Initial attempts have been completed to independently control the camera's rotating polarizer, and acquire images without the software intervention.

The interface code and initial instructions can be found on the lab's server (Becquerel > Tutorials and SOPs > GFP > GFP MATLAB Interface). Care should be exercised as software corruption and the rotating polarizer malfunctioning has been reported after attempting this approach.

CHAPTER

# 7

# CONCLUSIONS

In this contribution a summary of residual stress, and their origin on different crystallization methods was presented. Also, summaries of the fundamentals of photoelasticity and the IBI technique were described. Four wafers from different Si growth methods were subsequently evaluated with a combination of destructive and non-destrucive techniques.

The hypothesis of implementing IBI, paired with a continuous sectioning technique, proved to be suitable for imaging the residual stress spatial distribution, and for quantifying and decoupling residual stress components.

The results obtained in this work are in agreement with other previously reported residual stress results generated from different techniques and approaches. Moreover, values for quasi-mono residual stress in comparison to other methods were presented for the first time, to the author's best knowledge.

A series of alternative approaches to follow this work were recommended and initial steps towards expanding the presented studies were also demonstrated.

In summary, combining the current non-destructive IBI technique with a destructive sectioning method provides a potential approach to survey wafers from different growth systems that could be used for solar cell applications.

# APPENDICES

# Appendix A. Tool Calibration Steps

These steps are transcribed from S.Schoenfelder's Gray Field Polariscope document in the GFP computer. The notes were taken from instruction steps given by John Lesniak (Stress Photonics).

1. Switch on the light source fans and the camera and let heat up the system (~ 15 min).

2. Open the "PSA Calibration Page" and choose "Camera Units" as Output data.

3. Start camera imaging with the "GFP Control Panel".

4. Install band pass filters. Pay respect to the right direction! (*e.g.* the narrow band pass filter should be placed with the reflective side to the light source)

5. Adjust the light: The light image gives a representation of the light intensities. It should be in range of 200 – 400 A/D for the measuring area. It should not be too much light that the image represents a grey field.

6. Adjust the polarizer in the lighthouse until 30 A/D or less in Shear Max is reached. The polarizer consists of on linear polarizer and two 1/4λ wave plate (275nm retardation for each plate). By turning the wave plate the linear polarized light is adjusted to the wave plates, (*i.e.*, the flashing in the image is reduced). By turning the two wave plates to each other the circular polarization is adjusted to the measuring wavelength. If they stand perpendicular to each other all light is canceled out. If they are in the same direction 275 + 275 = 550 nm retardation can be achieved for a wavelength of 2200 nm. Thus, an optimal 1/4λ retardation can be achieved for every wavelength.

7. Place the calibration plate (275 nm) in the camera image with the stripes from front to back (one can use a sheet with straight edges to adjust the marks of the wafer plate at the edge; the edge can be aligned in the image parallel to one edge)

**8.** Capture image and the direction plot should show 90 within the calibration plate. In System > Preferences > GFP Configure the Direction Adj. can be adjusted to correct the angle of direction.

**9.** Switch to shear max result and average the signal within the calibration plate by drawing a box. Open the "PSA Calibration Page" and enter the average shear max signal value in "Peak Values". Set it as default with the menu bar within the page.

**10.** Save the configuration or calibration with: System > User Configure > Save As ...

**11.** Set "Retardation" as default in calibration page.

# Appendix B. Four Point Bending Device

The setup shown in Figure B.1 consists of two rectangular plates with spaced contact points for bending of the Si sample. The contact points are aluminum cylinders that have been fitted to the exact dimensions of the drilled holes. Hence, a degree of press fitting was required.

The contact points (*i.e.*, rods) were spray coated with Boron Nitride to reduce friction between them and the Si sample upon loading.

These dimensions were selected to complying as close as possible with ASTM D6272-10 (one half of support span) beam dimensions standards. As a demonstration, a (100) Si beam 300 μm thick, 70 mm long and 5 mm wide was cut and loaded, as seen in Figure B.2.

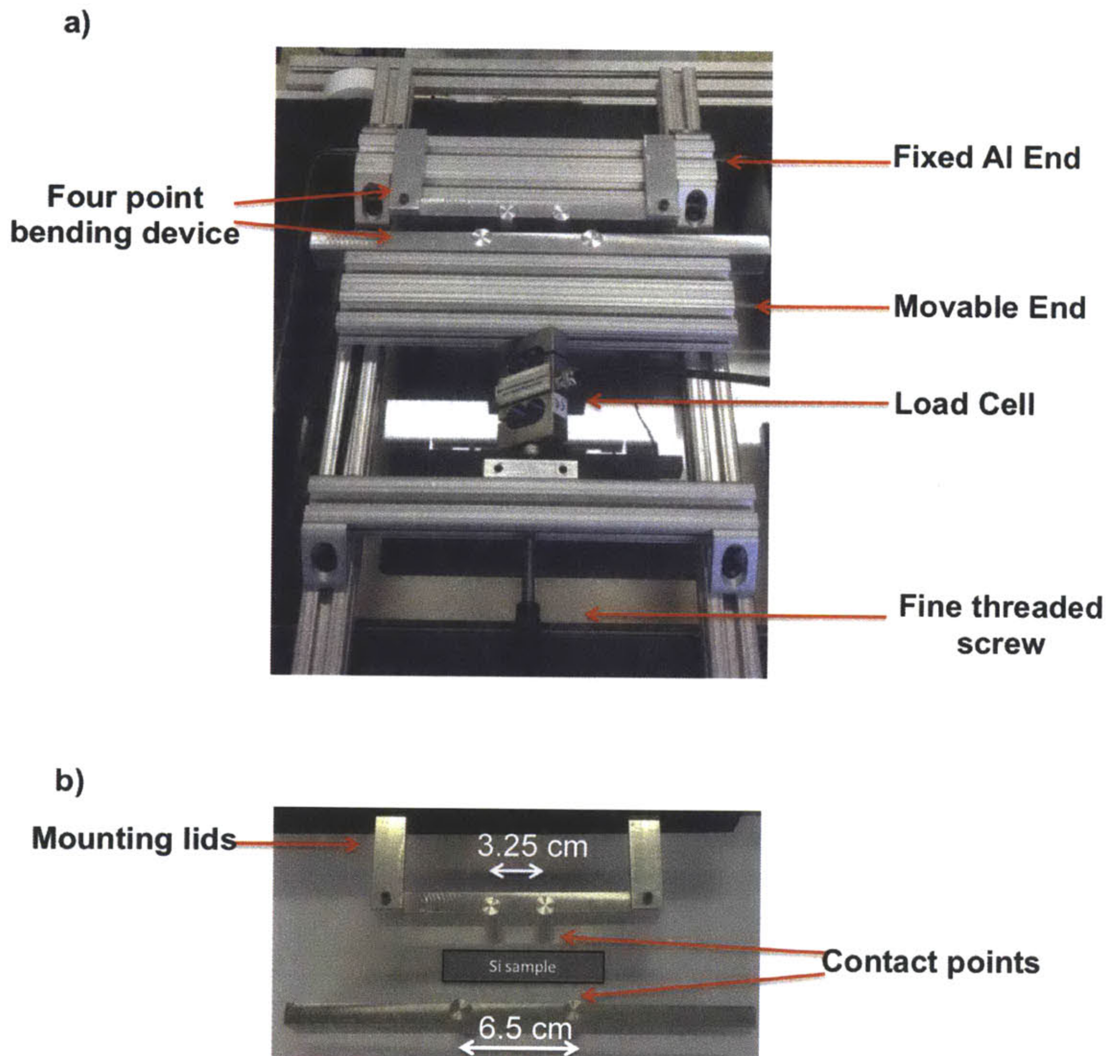


**Figure B 1 – Four point bending setup components. a) General setup area (load cell meter not shown), and b) Close up on the bending jig**

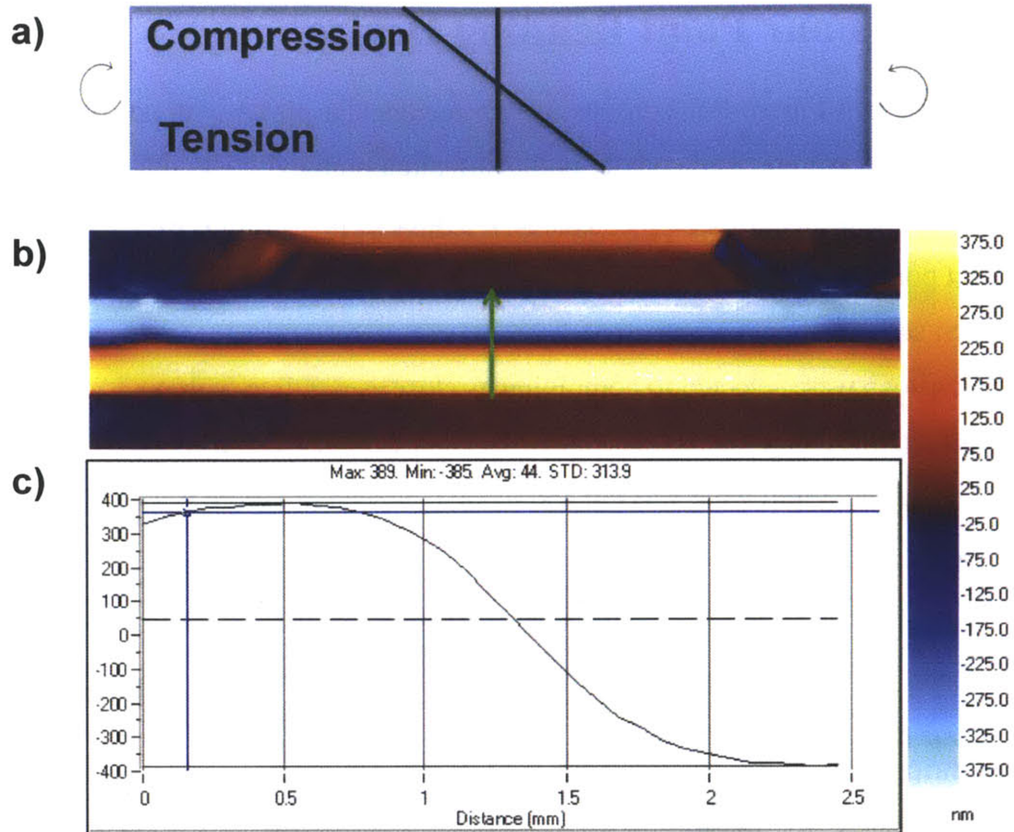


**Figure B 2 - a) Beam behavior under four point bending. Line shows the linear stress distribution expected. b) IBI image showing the difference in stress (color-coded) upon loading. c) Line scan from arrow in b) showing the expected stress state transition from a)**

# Appendix C. Height Impact on Spatial Resolution and Turning On Procedure

## C.1 Height Impact on Spatial Resolution

The change in camera height impacts the imaging spatial resolution. The graph shown below represents the impact on the resolution (μm/pixel), as a function of the distance between the end of the camera lens, and the glass where the sample is located.

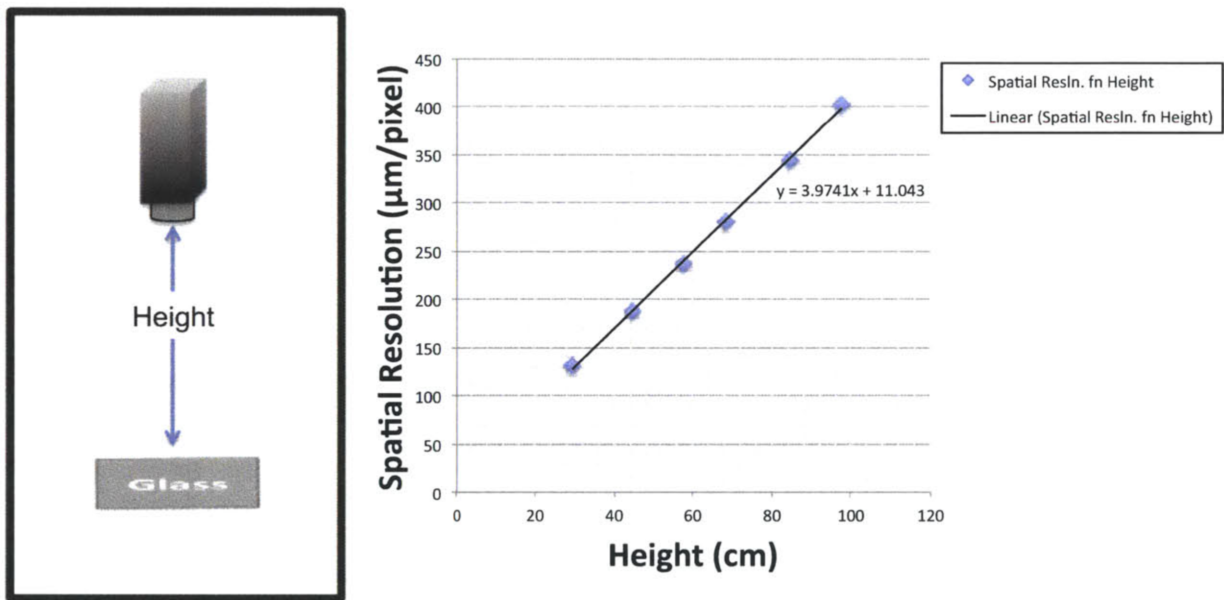


**Figure C 1 - Spatial resolution of imaged area as a function of camera height**

The camera can only go down to a certain distance, as shown in the first data point on the left in Figure C 1. Increasing the spatial resolution requires the use of an alternative 5x objective lens, which can capture features with a resolution of 5.6 μm/pixel.

## C.2 Tool turning on procedure

The effect of turning camera and source light on, and their order of operations permutations was tested to determine the optimal approach. The different permutations tested were:

A* = Leaving camera OFF, and turning light source ON for 15 min prior to imaging.

B* = Turning both camera and light source ON for 15 min prior to imaging.

C* = Turning light OFF but leaving camera ON prior to imaging.

The results are shown in Figure C.2.

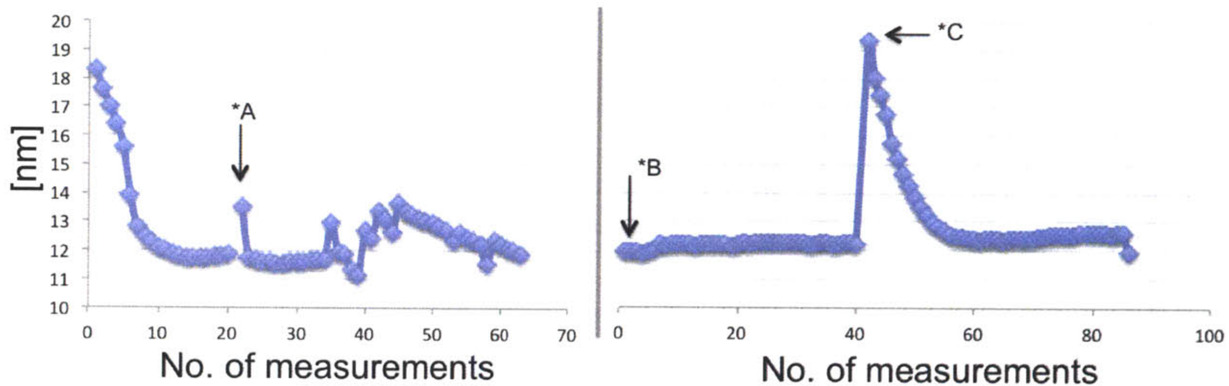


**Figure C 2 - Impact on retardation values of a background image due to the order of operations when turning equipment on**

From this experiment, it was determined that the procedure that would produce the least amount of spurious retardation values would be procedure B*; consisting on turning both camera and light source ON for 15 min to stabilize prior to imaging.

# Appendix D. DoE Laser Parameters

To test the parameters that would cut through a sample while introducing the least amount of stress (as measured by IBI), a design of experiment (DoE) was done analyzing the following four variables at three different levels:

i) Frequency

ii) Rate

iii) Laser pulse width

iv) Offset

The DoE lead to a $L_9$ array that reduced the work to 9 experiments, as opposed to a $3^4$=81 experiments, as seen in Figure D.1.

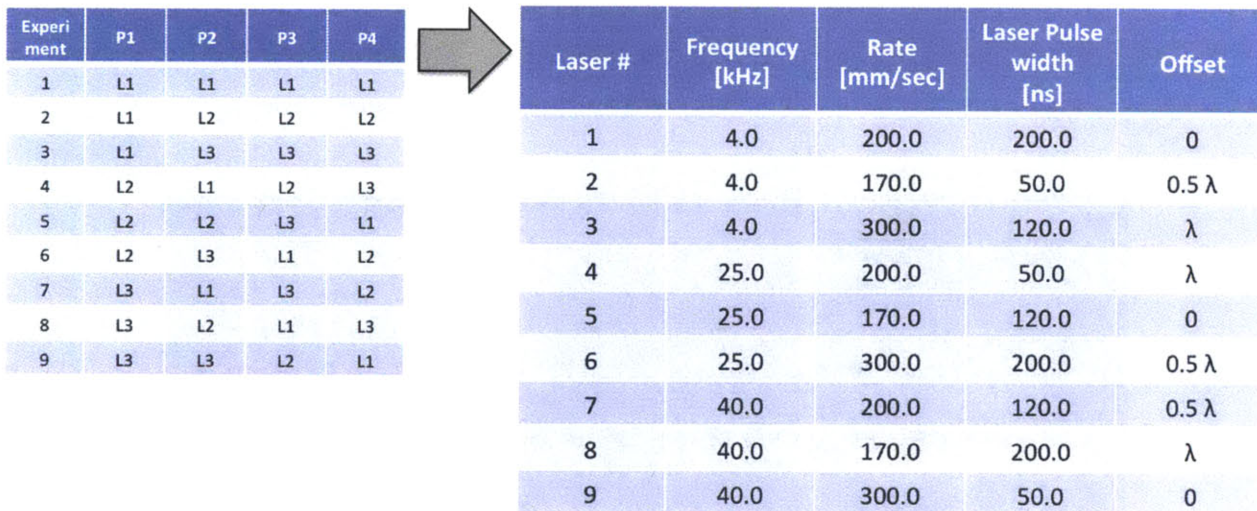

| Experiment | P1 | P2 | P3 | P4 |
|---|---|---|---|---|
| 1 | L1 | L1 | L1 | L1 |
| 2 | L1 | L2 | L2 | L2 |
| 3 | L1 | L3 | L3 | L3 |
| 4 | L2 | L1 | L2 | L3 |
| 5 | L2 | L2 | L3 | L1 |
| 6 | L2 | L3 | L1 | L2 |
| 7 | L3 | L1 | L3 | L2 |
| 8 | L3 | L2 | L1 | L3 |
| 9 | L3 | L3 | L2 | L1 |

| Laser # | Frequency [kHz] | Rate [mm/sec] | Laser Pulse width [ns] | Offset |
|---|---|---|---|---|
| 1 | 4.0 | 200.0 | 200.0 | 0 |
| 2 | 4.0 | 170.0 | 50.0 | 0.5 λ |
| 3 | 4.0 | 300.0 | 120.0 | λ |
| 4 | 25.0 | 200.0 | 50.0 | λ |
| 5 | 25.0 | 170.0 | 120.0 | 0 |
| 6 | 25.0 | 300.0 | 200.0 | 0.5 λ |
| 7 | 40.0 | 200.0 | 120.0 | 0.5 λ |
| 8 | 40.0 | 170.0 | 200.0 | λ |
| 9 | 40.0 | 300.0 | 50.0 | 0 |

**Table D.1 –DoE with Parameters and Levels varied in this study**

After performing the 9 cuts, they were subsequently imaged on IBI and cleaved to analyze the impact on the cross-section, as seen in Figure D.2 and D.3, respectively.

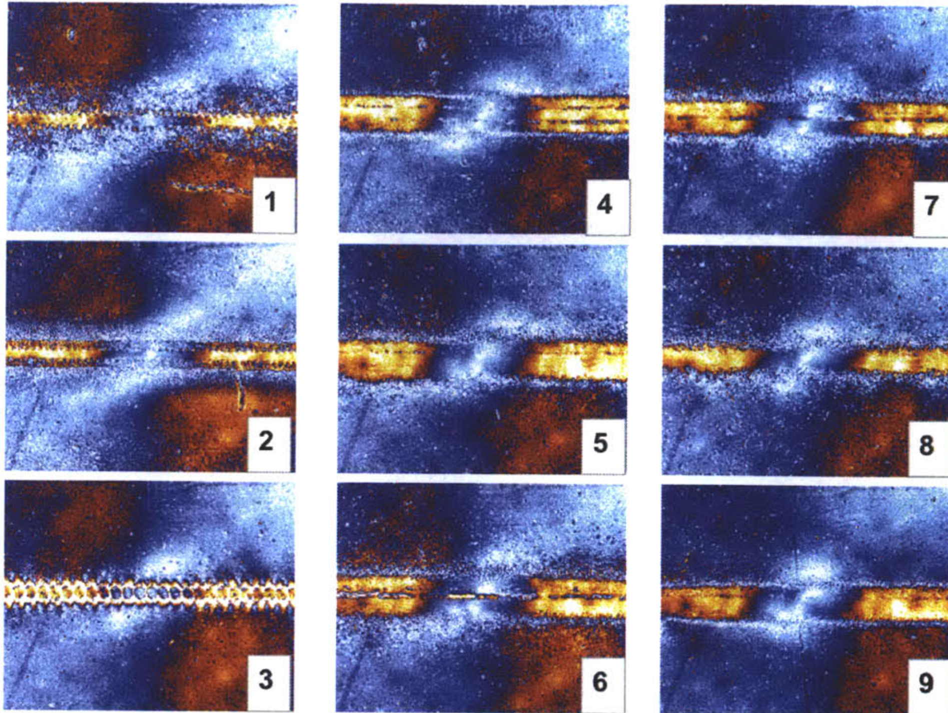


**Figure D 1 - IBI images of the 9 experiments from the laser optimization DoE**

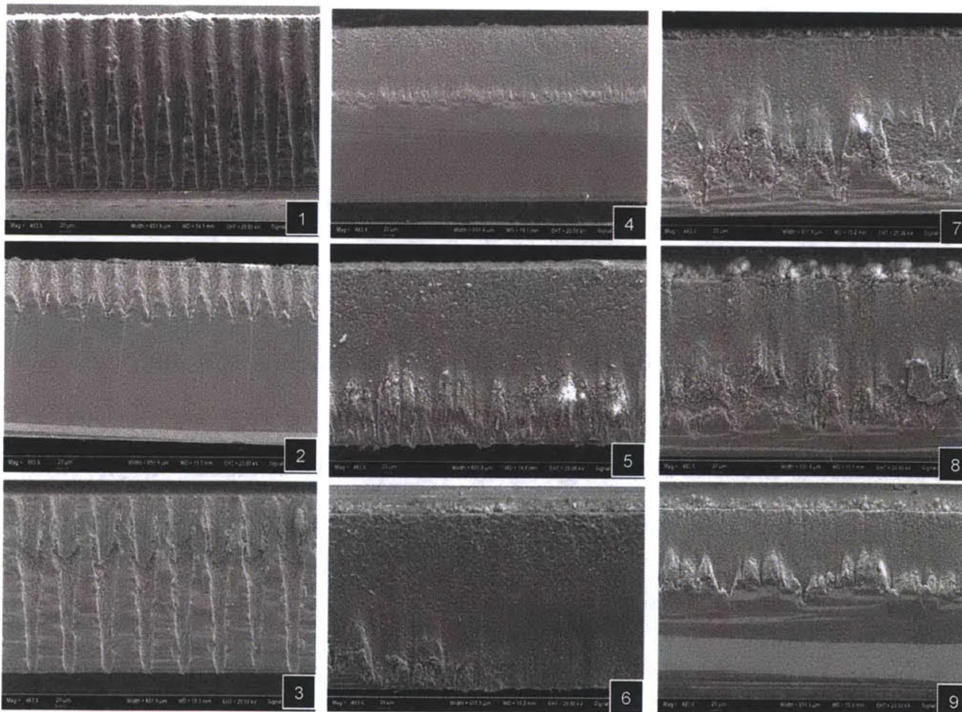


**Figure D 2 - Cross-sectional SEM images of the 9 experiments from the laser optimization DoE**

After obtaining the Signal/Noise ratio for each of the experiments, and following the DoE guidelines, the impact of each of the four different parameters (frequency, rate, pulse width, and offset) was analyzed, as shown in Figure D.4. The metric in this case was the minimum amount of retardation (or stress) measured at the cut lines.

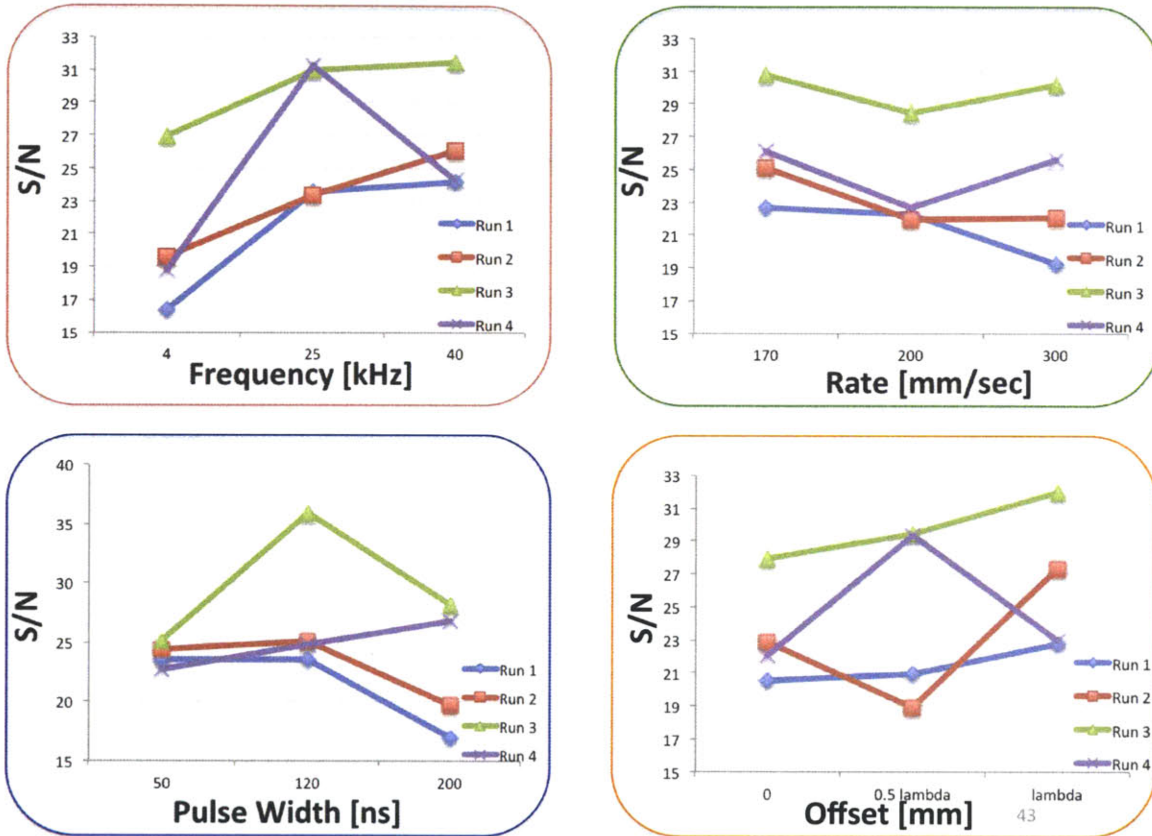


**Figure D 3 - Impact (S/N) from each of the parameters on the final stress values from lasering**

From Figure D.3 we observe that there are different trends from the experimental runs. Therefore, narrowing down the experimental work, three final parameters were selected based on the highest S/N ratios, and conventional procedures previously used, as shown in Table D.2.

**Table D.2 - Experimental parameters and retardation results for three different laser conditions**

## Experiments

| Sample | Frequency [kHz] | Rate [mm/sec] | Laser Pulse width [ns] | Offset |
|---|---|---|---|---|
| **1.1** = Overall Trend | 40 | 170 | 120 | λ |
| **1.2** = Purple DoE trend | 25 | 170 | 200 | 0.5 λ |
| **1.3** = Typical | 25 | 170 | 200 | 0 |

## Results

| 1.1 values [nm] | 1.2 values [nm] | 1.3 values [nm] |
|---|---|---|
| 2.84 | 3.18 | 3.03 |
| 3.05 | 3.09 | 3.38 |
| 2.94 | 3.25 | 3.03 |
| Avg.= 2.94 | Avg.= 3.17 | Avg.= 3.14 |

*Linescans taken from the Spray coated samples
**Values from boxed avg. over width of damage area.

Table D.2 shows the values from each of the three runs done on the three different sample conditions. The laser conditions from Laser Sample 1.1, that is, 40 kHz, 170 mm/sec, 120 ns, and offset of 1 μm was selected because of its average low retardation value. It is important to mention that the values from all three laser conditions are considered to be close to each other under any other practical terms. These values were acquired after rinsing the sample with water and soap, followed by a $N_2$ drying procedure.

The final IBI images from this experiment are shown in Figure D.4.

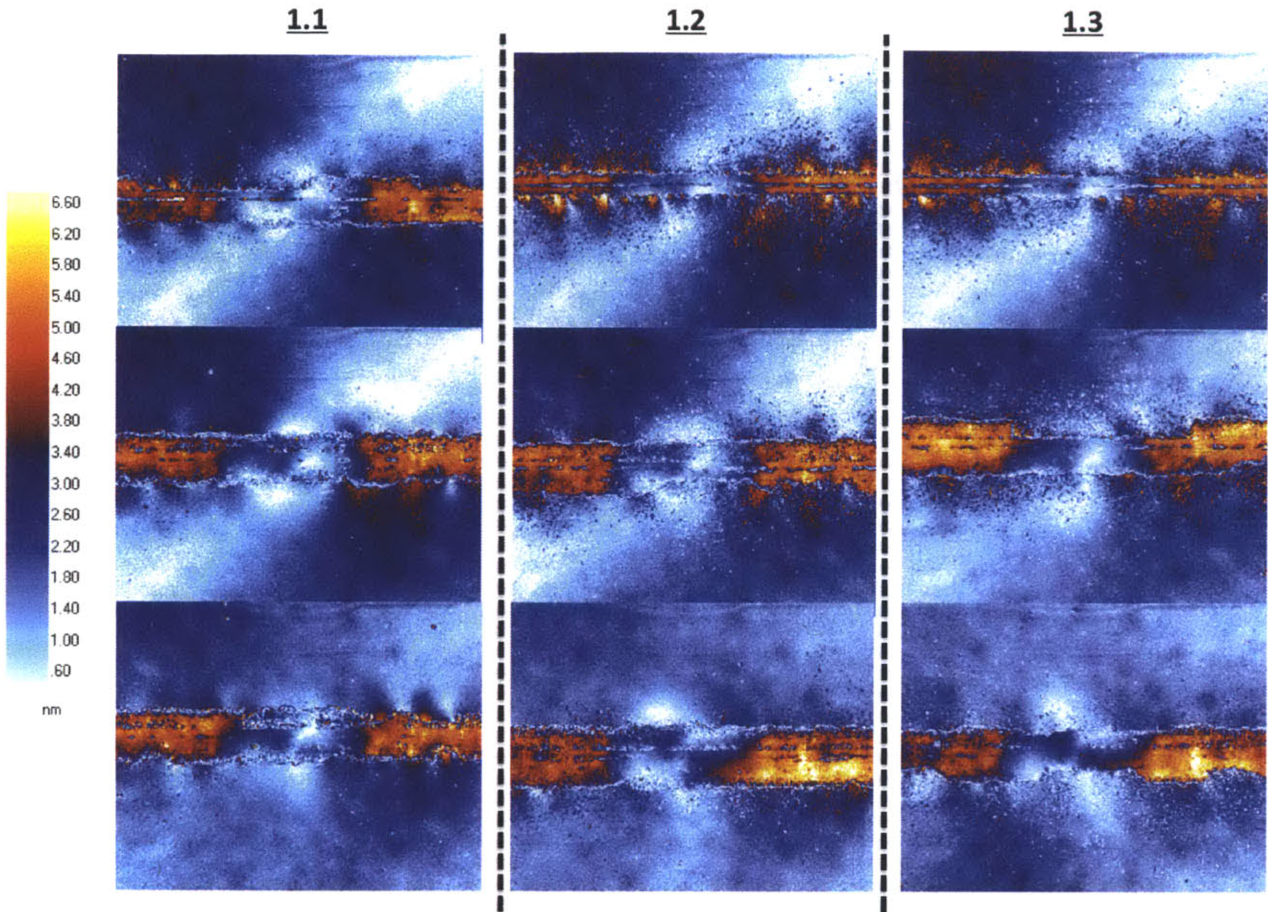


**Figure D.4 - IBI images of Final lasering optimization for samples 1.1, 1.2, and 1.3**

# REFERENCES


1 Morton, O.: *'Solar energy: A new day dawning?: Silicon valley sunrise'*, Nature, 2006, **443**, pp. 19-22

2 Muller, R.A.: *'Energy for Future Presidents'* (W.W. Norton & Company, 2012)

3 Kropp, R. (2009). *"Solar expected to maintain its status as the world's fastest-growing energy technology."* from http://www.socialfunds.com/news/article.cgi/2639.htmlS

4 Wilkinson, S.: *'Why crystalline PV remains king in a dynamic solar market'*, Solar Industry, 2011, **4**, (1), pp. 1

5 Powell, D.M., Winkler, M.T., Choi, H.J., Simmons, C.B., D. Berney Needleman, and Buonassisi, T.: *'Crystalline silicon photovoltaics: A cost analysis framework for determining technology pathways to reach baseload electricity costs'*, Energy and Environmental Science, 2012, **5**, pp. 5874-5883

6 Powell, D.M.: *'Simulation of Iron Impurity Gettering in Crystalline Silicon Solar Cells'*, Massachusetts Institute of Technology, 2012

7 del Cañizo, C., del Coso, G., and Sinke, W.C.: *'Crystalline silicon solar module technology: Towards the 1 € per watt-peak goal'*, Progress in Photovoltaics: Research and Applications, 2009, **17**, (3), pp. 199-209

8 Sopori, B.L., and Baghdadi, A.: *'Some investigations on the influence of defects/grain boundaries on photovoltaic mechanisms in polycrystalline silicon films'*, Solar Cells, 1979/80, **1**, pp. 237-250

9 Coletti, G., Bronsveld, P.C.P., Hahn, G., Warta, W., Macdonald, D., Ceccaroli, B., Wambach, K., Quang, N.L., and Fernandez, J.M.: *'Impact of Metal Contamination in Silicon Solar Cells'*, Advanced Functional Materials, 2011, **21**, pp. 879–890

10 Rinio, M., Yodyungyong, A., Keipert-Colberg, S., Borchert, D., and Montesdeoca-Santana, A.: *'Recombination in ingot cast silicon solar cells'*, physica status solidi (a), 2011, **208**, (4), pp. 760-768

11 Seifert, W., Morgenstern, G., and Kittler, M.: *'Influence of dislocation density on recombination at grain boundaries in multicrystalline silicon'*, Semiconductor Science and Technology, 1993, **8**, pp. 1687-1691

12 Seager, C.H.: *'Grain boundaries in polycrystalline silicon'*, Annual Review of Materials Science, 1985, **15**, pp. 271-302

13 Powell, D.M., Winkler, M.T., Goodrich, A., and Buonassisi, T.: *'Modeling the Cost and Minimum Sustainable Price of Crystalline Silicon Photovoltaic Manufacturing in the United States'*, IEEE Journal of Photovoltaics, 2013, **3**, (2), pp. 662-668

14 Möller, H.J., Funke, C., Rinio, M., and Scholz, S.: *'Multicrystalline silicon for solar cells'*, Thin Solid Films, 2005, **487**, pp. 179–187

15 Brun, X.F., and Melkote, S.N.: *'Analysis of stresses and breakage of crystalline silicon wafers during handling and transport'*, Solar Energy Materials and Solar Cells, 2009, **93**, (8), pp. 1238-1247

16 Withers, P.J., and Bhadeshia, H.K.D.H.: *'Overview: Residual Stress Part 1 - Measurement techniques'*, Materials Science and Technology, 2001, **17**, pp. 355-365

17 Rossini, N.S., Dassisti, M., Benyounis, K.Y., and Olabi, A.G.: *'Review: Methods of measuring residual stresses in components'*, Materials and Design, 2012, **35**, pp. 572-588

18 Luque, A., and Hegedus, S.: *'Handbook of Photovoltaic Science and Engineering'* (Wiley, 2011)

19 Moller, H.: *'Basic mechanisms and models of multi-wire sawing'*, Adv Eng Mater, 2004, **6**

20 McEvoy, A., Markvart, T., and Castaner, L.: *'Practical Handbook of Photovoltaics: Fundamentals and Applications'* (Academic Press, 2012)

21 L. Jester, T.: *'Crystalline Silicon Manufacturing Progress'*, Progress in Photovoltaics Research and Applications, 2002, **10**, pp. 99-106

22 T. Iwaki, N.K.: *'Residual stresses of czhochralski-grown crystal'*, Transactions of ASME, 1981, **48**

23 B. Wu, N.S., R. Ma, R. Clark: *'Bulk multicrystalline silicon growth for photovoltaic (PV) application'*, Journal of Crystal Growth, 2008, **310**, (7-9), pp. 2178-2184

24 M'Hamdi, M., Meese, E.A., Laux, H., and Øvrelid, E.J.: *'Thermo-Mechanical Analysis of Directional Crystallisation of Multi-Crystalline Silicon Ingots'*, Materials Science Forum, 2006, **508**, pp. 597-602

25 Franke, D., Rettelbach, T., Häßler, C., Koch, W., and Müller, A.: *'Silicon ingot casting: process development by numerical simulations'*, Solar Energy Materials and Solar Cells, 2002, **72**, (1–4), pp. 83-92

26 Stoddard, N., Wu, B., Witting, I., Wagener, M.C., Park, Y., Rozgonyi, G.A., and Clark, R.: *'Casting Single Crystal Silicon: Novel Defect Profiles from BP Solar's Mono2 TM Wafers'*, Solid State Phenomena, 2007, **131-133**, pp. 1-8

27 Barredo, J., Parra, V., Guerrero, I., Fraile, A., and Hermanns, L.: *'On the mechanical strength of monocrystalline, multicrystalline and quasi-monocrystalline silicon wafers: a four-line bending test study'*, Progress in Photovoltaics Research and Applications, 2013

28 Schmid, F.: *'Casting large silicon single-crystals'*, Journal of Electronic Materials, 1976, **5**, (436-437)

29 Gao, B., Nakano, S., and Kakimoto, K.: *'Influence of Back-Diffusion of Iron Impurity on Lifetime Distribution near the Seed-Crystal Interface in Seed Cast-Grown Monocrystalline Silicon by Numerical Modeling'*, Crystal Growth and Design, 2012, **12**, pp. 522-525

30 Chen, X.J., Nakano, S., Liu, L.J., and K.Kakimoto: *'Study on thermal stress in a silicon ingot during a unidirectional solidification process'*, Journal of Crystal Growth, 2008, **310**, pp. 4330-4335

31 Applied Materials: *'Wafer Wire Sawing Economics and Total Cost of Ownership Optimization'*, (White paper, 2011)

32 Wallace, R.L., Hanoka, J.I., Rohatgi, A., and Crotty, G.: *'Thin silicon string ribbon'*, Solar Energy Materials & Solar Cells, 1997, **48**, pp. 179-186

33 He, S.: *'Near Infrared Photoelasticity of Polycrystalline Silicon and it's Relation to In-Plane Residual Stresses'*, Georgia Institute of Technology, 2005

34 Anderoglu, O.: *'Residual stress measurement unsing x-ray diffraction'*, Texas A&M University, 2004

35 Belyaev, A., Polupan, O., Ostapenko, S., Hess, D., and Kalejs, J.P.: *'Resonance ultrasonic vibration diagnostics of elastic stress in full-size silicon wafers'*, Semiconductor Science and Technology, 2006, **21**, pp. 254-260

36 Schajer, G.S.: *'Relaxation Methods for Measuring Residual Stresses: Techniques and Opportunities'*, Experimental Mechanics, 2010, **50**, pp. 1117-1127

37 Hearn, E.J.: *'Photoelasticity'* (Merrow Technical Library, 1971)

38 Heywood, R.B.: *'Photoelasticity for designers'* (Pergamon Press, 1969)

39 Cramer, K.E.: *'A Stress Imager Integrating Thermoelastic and Photoelastic Stress Analysis'*, (NASA, The College of William & Mary, Stress Photonics, Contract No. NAS1-97036, 2000)

40 Hendry, A.W.: *'Photoelastic Analysis'* (Pergamon Press, 1966)

41 Horn, G., Lesniak, J., Mackin, T., and Boyce, B.: *'Infrared grey-field polariscope: A tool for rapid stress analysis in microelectronic materials and devices'*, Review of Scientific Instruments, 2005, **76**, pp. 045108

42 Ramesh, K.: *'Digital Photoelasticity - Advanced Techniques and Applications'* (Springer, 2000)

43 Brito, M.C., Alves, J.M., Serra, J.M., Gamboa, R.M., Pinto, C., and Vallera, A.M.: *'Measurement of residual stress in multicrystalline silicon ribbons by a self-calibrating infrared photoelastic method'*, Review of Scientific Instruments, 2005, **76**, pp. 013901

44 Ganapati, V., Schoenfelder, S., Castellanos, S., Oener, S., Koepge, R., Sampson, A., Marcus, M.A., Lai, B., Morhenn, H., Hahn, G., Bagdahn, J., and Buonassisi, T.: *'Infrared birefringence imaging of residual stress and bulk defects in multicrystalline silicon'*, Journal of Applied Physics, 2010, **108**, (6), pp. 063528

45 Stress Photonics. "Stress Photonics: Delta Vision Software." on http://stress .com/PSA/PSA_Intro.html, Accessed 01/14 2014

46 A.J. Matchett, J.C.O.N., A.P. Shaw: *'Stress distribution in 2-dimensional wedge hoppers with circular arc stress orientation: a coordinate specific Lame-Maxwell model'*, Powder Technology, 2008, **187**

47 T. Liu, A.A., CG Boay: *'Full field automated photoelasticity using two-load-step method'*, Optical Engineering, 2001, **40**

48 G. Petrucci, G.R.: *'Automated stress separation along stress trajectories'*, Experimental Mechanics, 2007, **47**, pp. 733-743

49 M. Fukuzawa, R.K., M. Yamada, T. Hirasawa: *'Residual strain distribution in casting ingot of multi-crystalline silicon'*, Energy Procedia, 2011, **3**, pp. 13-16

50 K.A. Dumas, A.B., L.J. Cheng: *'Annealing effects in low- and high-stress silicon ribbon'*, MRS Proceedings, 1985, **59**

51 J. Li, I.K., V. Prasad: *'Modeling Stresses of Contacts in Wire Saw Slicing of Polycristalline and Crystalline Ingots: Application to Silicon Wafer Production'*, Journal of Electronic Packaging, 1998, **120**

52 Mau, C.: *'Control of Wafer-scale Non-uniformity in Chemical-Mechanical Planarization by Face-up Polishing'*, Massachusetts Institute of Technology, 2008

53 R.E. Ogilvie, U.K., H. Sugiyama, J. Nicolich: *'X-Ray stress analysis employing the lattice parameter ellipsoid'*, JCPDS International Centre for Diffraction Data 2007

54 E. Sachs, D.E., J. Serdy: *'Edge stabilized ribbon (ESR) growth of silicon for low cost photovoltaics'*, Journal of Crystal Growth, 1987, **82**, pp. 117-121

55 Ravi, K.: *'The growth of EFG silicon ribbons'*, Journal of Crystal Growth, 1977, **39**, (1), pp. 1-16

56 Garcia, D., Ouellette, M., Mackintosh, B., and Kalejs, J.P.: *'Shaped crystal growth of 50 cm diameter silicon thin-walled cylinders by edge-defined film-fed growth (EFG)'*, Journal of Crystal Growth, 2001, **225**, (2-4), pp. 566-571

57 Moller, H.J.: *'Carbon-Induced twinning in multicrystalline silicon'*, Solid State Phenomena, 2004, **95-96**, pp. 181-186

58 Fukuzawa, M., Yamada, M., Islam, M.R., Chen, J., and Sekiguchi, T.: *'Quantitative Photoelastic Characterization of Residual Strains in Grains of Multicrystalline Silicon'*, Journal of Electronic Materials, 2010, **39**, (6), pp. 700-703

59 Kalpakjian, S., and Schmid, S.R.: *'Manufacturing processes for engineering materials'*, Pearson Education, 2010

60 Hull, D., and Bacon, D.J.: *'Introduction to dislocations'*, Oxford: Butterworth-Heinemann, 2011

61 Wortman, J.J., and Evans, R.A.: *'Young's modulus, shear modulus, and Poisson's ratio in silicon and germanium'*, J. Appl. Phys., 1965, **36**, pp. 153-156

62 Finnie, S.V.I.: *'Determination of residual stresses from stress intensity factor measurements'*, Transactions of the ASME, 1971, pp. 242-246